**VKI, von Karman Institute for Fluid Dynamics,**
**Lecture Series Programme 1999–2000,**
**"Theoretical and Experimental Modeling of Particulate Flow"**
**Bruessels, Belgium, 03.–07. April 2000.**

# Application of Eulerian–Lagrangian Prediction of Gas–Particle Flows to Cyclone Separators

**Dr. Th. Frank**

University of Technolgy Chemnitz
Faculty of Mechanical Engineering and Process Technology
Research Group on Multiphase Flow
09107 Chemnitz, Germany
Phone: +49 371 531 4643
Fax: +49 371 531 4644
E-Mail: frank@imech.tu-chemnitz.de

SIVUS gGmbH, Chemnitz
Institute of Process / Environmental Engineering and Sensor Technology
CFD Applications Group
Schulstrasse 38
09125 Chemnitz, Germany

## 1 Introduction

The cyclone separator has already been invented more then 100 years ago by Morse in 1886 for the Knickerbocker Company [28]. Today the cyclone in its various designs is perhaps the most widely used dust collection device to be found in industry. It owes its popularity to the high reliability in operation and the low manufacturing and maintainance costs brought about by its simple and compact mechanical design. There are no moving parts in the device itself, and they can be constructed of a wide range of materials, which does not preclude the use of refractories for high–temperature operation. Combined with the moderate pressure drop and a range of throughputs and efficiencies, these advantages have made the cyclone the most attractive solution to separation requirements in the reduction of all types of pollutants emissions, for powder handling, catalyst recovery, and for combined cycle power generation. Where the cyclone cannot provide the requisite efficiency, it may still be used to advantage in conjunction with higher–efficiency collection devices, such as electrostatic precipitators or filters.

Cyclones can be distinguished from other seperation devices by nothing that the streamlines complete several revolutions about the axis, the "centrifugal" forces so produced being the means of separation. In the familiar reverse–flow cyclone of the cylinder–on–cone design, which is shown diagrammatically in Fig. 1, gases spiral down from a tangential (or spiral) inlet, towards the apex of a conical section where the flow is reversed and particles are collected in a hopper. The gases then proceed upwards in an inner core of fluid towards the gas exit via the vortex finder. Superimposed onto this simplified picture are a multitude of complex gas–particle and particle–particle interactions including sliding and non–sliding particle–wall collisions (with or without wall roughness effects), reentrainment of particles from the hopper, turbulent particle dispersion, turbulence suppression by the particles as well as particle milling and agglomeration.

Cyclone design has proceeded over all the years since its invention. Also if today there are a large number of different designs for various industrial applications (see Fig. 3 and

4), its most basic form the device has changed little over a century of service. There have been many attempts to improve its performance by modifying the boundary conditions, introducing auxilliary injection via vanes or stationary propellers, incorporating vortex stabilizing baffles and recirculating devices, and by employing many small cyclones in one unit called "multicyclones" (see Fig. 4). These devices have met with varying degrees of success, and the manufacturers claims for these have not always been reproduced in plant operation.

A considerable amount of experimental data exists on cyclone performance, obtained for the most part in 1930s and 40s using impact tubes, before the availability of laser–doppler anemometry or electronic hot–wire probes, which forms the basis of many necessarily semi–empirical correlations on which current cyclone design practice is almost entirely based. Only in recent years laser–doppler and phase–doppler anemometry techniques has been applied to cyclone flow in order to measure all 3 gas velocity components with a sufficient resolution [17] e.g. for improvement of cyclone design and for comparison with modern numerical methods.

The semi–empirical design methods shown in the following sections in theire basic outline usually rest on a number of expressions to obtain an overall pressure drop and a characteristic grade–efficiency curve, as a function of geometrical factors and operating conditions. The application of these "theories" lead to a number of "optimized" designs for any specific application, from which one must be chosen on economic grounds.

The existence of this varity of semi–empirical methods shows the lack of a rigorous design method. It is widely accepted that the performance of mechanical separators such as the cyclone are capable of meeting more stringent requirements than are presently achieved. The lack of a fundamental understanding of the separation process which could lead to such improved performance is due to the fact that despite their apparent simplicity, the fluid dynamics of cyclones are complex including such features as high preservation of vorticity and in some cases several annular zones of forward– and reverse–moving streams.

The problem associated with mathematical modelling of the detailed flow patterns involves the solution of the strongly coupled, nonlinear partial differential equations of the conservation of mass and momentum, and lies well beyond any forseeable analytical approach. A numerical approximation must therefore be adopted, which necessitates a suitable turbulence model to avoid an impracticably large amount of calculation. The mathematical basis of the general procedure is given in the following sections. Firstly, the conservation equations for the gas phase are presented. This is followed by the used equations of motions of the dispersed phase given in a Lagrangian frame of reference and a short outline of the solution algorithm for both the gas and disperse phase equations of motion. Finally the numerical method is applied to standard cyclone and so called symmetrical double cyclone separators, and the predicted results are compared with the experimental data as far as they were available for the different investigated cyclone separator designs.

# 2 Semi–empirical Models for Cyclone Design

## 2.1 Flow Patterns

Cyclone performance is evaluated in terms of pressure drop and collection efficiency. To assess factors that contribute to performance, cyclone flow patterns must be understood. The dominant flow pattern consists of an outer vortex spiraling downward along the cyclone walls (Fig. 5). This vortex is created when the gas stream enters the cyclone tangentially or axially through swirl vanes. As the gas spiral reaches below the gas outlet duct, gas begins to flow radially inward from the outer vortex toward the cyclone axis. The gas that flows inward forms an inner vortex or central core. Although the core rotates in the same direction as the outer vortex, the gas spins upward to the gas outlet. Collection takes place as particles in the outer vortex are thrown to the cyclone walls by centrifugal force. These particles slide down the walls of the cyclone to the dust hopper aided by the downward movement of the gas near the wall. Already in the case of moderate particle loadings formation of a paricle rope may occure in the region near the cyclone wall. Particles drawn into the central core are not collected and leave the apparatus together with the clean gas through the vortex finder.

Gas motion in the cyclone can be described in terms of tangential, radial and axial (vertical) velocity components (Fig. 5). Ter Linden's [41] measurements of these components are shown in Fig. 2.a)–2.c). Gas flow in industrial sized cyclones is turbulent. Thus each of the three velocity components is subject to turbulent fluctuations that are difficult to quantify, but that can influence particle collection greatly.

Tangential gas velocity in the outer vortex increases from a minimum value near the wall to a maximum at the edge of the central core (Fig. 2.a) and can be described by :

$$v_{F,t} \cdot r^n = const. \tag{1}$$

where $v_t$ is the tangential velocity and $r$ is the radial distance from the cyclone axis. The vortex exponent $n$ has been measured in the range of 0.5 to 1.0 for clean gas and varies in dependence on gas–inlet design, geometrical properties of the cyclone, particle loading and gas inlet velocity. Alexander [1] gives an empirical expression to calculate $n$ for any cyclone diameter $D$ and gas temperature $T$ :

$$n = 1 - \left[ (1 - 0.67 D^{0.14}) \left( \frac{T}{283} \right)^{0.3} \right] \tag{2}$$

In the outer vortex, tangential velocity can greatly exceed the cyclone inlet velocity.

Fig. 2.a) also shows that the tangential velocity decreases within the central core, falling to near zero at the cyclone axis. In the core gas rotates more nearly as a solid body. Thus tangential velocity in the core region can be described by :

$$\frac{v_{F,t}}{r} = \omega = const. \tag{3}$$

where $\omega$ is the rotational velocity of the central core vortex. At the top the cyclone the diameter of the central core is approximatly the same as the gas outlet diameter; near the bottom it is much narrower. Different ratios for the core diameter in respect to the clean gas outlet diameter have been assumed in literature ranging from 0.5 to 1.0. The core diameter is a key parameter in calculating collection efficiency according to the static particle method presented in the following.

Fig. 2.b) shows ter Linden's [41] measurements of radial gas velocity in the cyclone. This figure indicates a relatively small and constant inward radial velocity in the outer vortex at all vertical positions below the gas outlet duct. However other measurements have shown that this velocity component can vary over the height of the cyclone. In this case large radial velocities directed inward directly below or near the gas outlet can substantially decrease cyclone separator performance.

Vertical gas velocity measurements (Fig. 2.c) show that gas flow is downward near the cyclone wall. This downward velocity, rather than gravity, is largely responsible for conveying dust from the cyclone wall to the dust bin. As shown in Fig. 2c) the transition from downward to upward gas movement takes place outside the central core. Once gas enters the core, its upward velocity increases substantially.

## 2.2 Collection Efficiency

Collection efficiency is defined as the fraction of particles of any given size that are retained by the cyclone :

$$T(d_P) = 1 - \frac{\dot{m}_{out}(d_P)}{\dot{m}_{in}(d_P)} = 1 - \frac{\dot{N}_{out}(d_P)}{\dot{N}_{in}(d_P)} \tag{4}$$

where $\dot{m}(d_P)$ and $\dot{N}(d_P)$ are the particle mass flow rate and the particle number flow rate for a given particle size in the inlet and gas outlet cross section respectively. The efficiency of particle collection $T(d_P)$ by an inertial seperator of given geometrical dimensions, operated at given gas properties and throughput, depends on particle diameter $d_P$ and density $\rho_P$. When efficiency is plotted against particle size, the result is the fractional or grade efficiency curve for the cyclone (Fig. 6 shows a typical example). The particle size which can be collected by a cyclone is commonly expressed in terms of the particle cut size $d_{P,50}$, i.e. the particle size which is collected (at low particle loading) with 50 % efficiency, $T(d_{P,50}) = 0.5$.

Several theoretical approaches exist for prediction of the cyclone efficiency. By making different simplifying assumptions about the gas flow through the cyclone, different authers arrive at various approximate solutions for the determination of the particle cut size or the grad efficiency curve for a given cyclone separator design. Due to the impact of different cyclone designs and operation conditions on the validity of the made assumptions and simplifications, no single theory is likely to predict cyclone efficiency accurately for all applications. In general, three different theoretical approaches for the determination of cyclone efficiency can be identified.

### 2.2.1 Critical Diameter : Static Particle Approach

Separation of particles in cyclones occurs mainly due to centrifugal force caused by the spinning gas stream. The static particle approach determines the particle diameter for which centrifugal and buoyancy (Archimedes) force acting on the particle is exactly balanced by the drag force from gas that flows radially inward to the cyclone core. For these particles, radial acceleration and velocity ar zero, so the particles should rotate indefinitly around the edge of the core. Drag force on smaller particles with the same density exceeds centrifugal force. So they are carried by fluid flow into the cyclone core and leave the cyclone through the clean gas exit. Larger particles are moving towards the cyclone wall following there outward radial acceleration by the larger centrifugal force. After separation these particles are carried by the downward gas stream to the dust hopper and can be collected there.

For the balance of forces acting on a particle moving in a distance $r$ from the cyclone axis (neglecting other inertial, Coriolis, Magnus, Saffman and gravitational forces) we can write :

$$\vec{F_C} + \vec{F_D} + \vec{F_A} = 0 \tag{5}$$

where $\vec{F_C}$ is the centrifugal force, $\vec{F_D}$ is the drag force and $\vec{F_A}$ is the buoyancy force. The drag force acting in the direction of the relative velocity between the gas and the particle $\vec{v}_{rel} = \vec{v_F} - \vec{v_P}$ is the only force in equation (5) which could have a tangential component. So it can be directly deduced from the force balance ($F_{D,t} = 0$) that a particle which is stationary spinning around the edge of the vortex core moves with the same tangential velocity as the fluid :

$$v_{P,t} = v_{F,t} \tag{6}$$

For a particle rotating with the same speed as the tangential gas velocity at radial position $r$, the centrifugal force is :

$$F_{C,r} = \rho_P \frac{\pi}{6} d_P^3 \, r\omega^2 \tag{7}$$

The buoyancy force is acting radial inward :

$$F_{A,r} = -\rho_F \frac{\pi}{6} d_P^3 \, r\omega^2 \tag{8}$$

and for the radial component of the drag force we can write :

$$F_{D,r} = -\frac{\rho_F}{2} \, C_D(Re_P) \, \frac{\pi}{4} \, d_P^2 \, v_{rel}^2 \tag{9}$$

Assuming Stokes law for the drag coefficient $C_D$ :

$$C_D = \frac{24}{Re_P} = \frac{24\mu}{\rho_F \, d_P \, v_{rel}} \tag{10}$$

we are able to calculate from equation (5) the radial realtive particle velocity :

$$v_{rel}^2 = \frac{4}{3} \frac{\rho_P - \rho_F}{\rho_F} d_P \frac{1}{C_D(Re_P)} r\omega^2 \tag{11}$$

Using the solid body assumption for the core vortex inside the radial position r we can substitute the rotational velocity $\omega = v_{F,t}(r)/r$. With equation (10) we can express the relative particle velocity in radial direction as :

$$v_{rel} = \frac{(\rho_P - \rho_F) \, d_P^2}{18\mu} \, \frac{v_{F,t}(r)}{r} \tag{12}$$

Further it is assumed that for a particle of the critical cut diameter $d_T$, which is indefinitly rotating around the edge of the cyclone core, the relative particle velocity is equal to the radial inward gas velocity ($v_{rel} = v_{F,r}(r)$). From that follows :

$$d_T = \sqrt{\frac{18\mu}{\rho_P - \rho_F}} \sqrt{\frac{r \cdot v_{F,r}(r)}{v_{F,t}^2(r)}} \tag{13}$$

Existing theoretical approaches differ in the way how they define the radius of the cyclone core and in the determination of the gas velocity components at the edge of the vortex core.

**Method 1 :**

One of the most commonly applied methods for the determination of cyclone efficiency is the theory of Muschelknautz [30] which is based on the model of Barth [3]. It can also be found in secondary literature as e.g. in [22, 38]. In this method it is assumed, that the design and the geometrical properties of certain type of cyclones can be characterized by experimentally obtaining the relation between the tangential gas velocity on the edge of the core vortex $v_{F,t}(r)$ and the mean gas velocity in the outlet cross section of the vortex finder $v_i$ :

$$U = \frac{v_{F,t}(r)}{v_i} \qquad \text{with :} \qquad v_i = \frac{\dot{V}}{\pi r_i^2} \tag{14}$$

where $\dot{V}$ is the volume flow rate of the gas through the cyclone and $r_i$ is the radius of the vortex finder tube. Furthermore assuming that the radius of the core vortex of the cyclone is constant over the height of the cyclone and is equal to the radius $r_i$ of the vortex finder, the radial gas velocity $v_{F,r}(r)$ can also be predicted from the gas volume flow rate :

$$v_{F,r}(r) = \frac{\dot{V}}{2\pi\, r_i h_i} \tag{15}$$

where $h_i$ is the height of the cylindrical surface of the core vortex. From that assumptions for critical cut diameter $d_T$ follows from equations (13), (14) and (15) :

$$\begin{aligned} \frac{r \cdot v_{F,r}(r)}{v_{F,t}^2(r)} &= \frac{r_i \dot{V}}{U^2\, v_i^2\, 2\pi\, r_i h_i} \\ &= \frac{\dot{V}}{U^2\, v_i^2\, 2\pi h_i} \\ &= \frac{\dot{V}\pi^2 r_i^4}{U^2\, 2\pi\, h_i\, \dot{V}^2} \\ &= \frac{\pi r_i^3}{U^2\, 2\, h_i/r_i\, \dot{V}} \end{aligned}$$

$$\Longrightarrow \qquad d_T = \sqrt{\frac{9\mu}{\rho_P - \rho_F}}\, \frac{1}{U\sqrt{h_i/r_i}}\, \sqrt{\frac{\pi r_i^3}{\dot{V}}} \tag{16}$$

In accordance with the theory of Muschelknautz [38] the relationship for $U$ can be expressed in the form :

$$U = \left(\alpha \frac{F}{R_e} + \lambda H\right)^{-1} \tag{17}$$

with

$$F = \frac{A_e}{A_i} = \frac{ab}{\pi r_i^2} \quad , \quad R_e = \frac{r_e}{r_i} \quad , \quad H = \frac{h}{r_i} \tag{18}$$

where $F$, $R_e$ and $H$ represent the cyclone geometry (see Fig. 7) and the coefficients $\alpha$ and $\lambda$ has to be determined experimentally for each different type of cyclone separator. Then the grade efficiency curve can be predicted [38] with :

$$\begin{aligned} T(d_P) &= \left(1 + 2.0/(d_P/d_T)^{3.564}\right)^{-1.235} \qquad \text{for tangential inflow, curve a) Fig. 6} \\ T(d_P) &= \left(1 + 9.14/(d_P/d_T)^{5.3}\right)^{-0.53} \qquad \text{for spiral inflow, curve b) Fig. 6} \end{aligned} \tag{19}$$

**<u>Method 2 :</u>**

In [45] another theory for the prediction of the gas velocities $v_{F,t}(r)$ and $v_{F,r}(r)$ can be found, which is based on the work of Trefz [42] and Muschelknautz [32] taking into account the secondary flow in the cyclone along the outer wall of the vortex finder as well as higher particle loading. In this theory it is assumed that an amount of $0.1 \cdot \dot{V}$ of the total gas volume flow rate is recirculating along the wall of the vortex finder and only a flow rate of $0.9 \cdot \dot{V}$ is crossing the cylindrical surface of the vortex core below the inlet cross section of the vortex finder. This ratio for the secondary flow is a mean value and can be vary from 5–15 % in dependence on the particle loading. Furthermore the tangential velocity at the vortex finder is assumed to be only $v_{F,t}(r) = \frac{2}{3}u_i$ (with $u_i$ – the tangential velocity at radius of the gas outlet/vortex finder) due to the boundary layer flow along the wall of the vortex finder. Under these assumptions we can write :

<u>for the region of secondary flow</u>

$$r \cdot v_{F,r}(r) = \frac{0.1\dot{V}}{2\pi s}$$

$$v_{F,t}(r) = \frac{2}{3}u_i$$

$$d_T = \sqrt{\frac{9\mu}{\rho_P - \rho_F}}\sqrt{\frac{0.1\dot{V}}{\left(\frac{2}{3}u_i\right)^2 \pi s}}$$

<u>for the main flow region (vortex core)</u>

$$r \cdot v_{F,r}(r) = \frac{0.9\dot{V}}{2\pi h_i}$$

$$v_{F,t}(r) = u_i$$

$$d_T = \sqrt{\frac{9\mu}{\rho_P - \rho_F}}\sqrt{\frac{0.9\dot{V}}{u_i^2 \pi h_i}} \tag{20}$$

In accordance with [45] the cyclone shows an optimum performance, if both particle cut sizes predicted from equations (20) show the same value. In this case we get for the height of intrusion of the vortex finder :

$$s = 0.25\, h_i \tag{21}$$

Following Trefz and Muschelknautz [45, 31] the tangential gas velocity $u_i$ can be predicted from :

$$u_i = \frac{u_a\, r_a/r_i}{1 + \frac{1}{2}\,\lambda_S\,\frac{A_R}{\dot{V}}\,u_a\sqrt{\frac{r_a}{r_i}}} \tag{22}$$

where $A_R$ is the whole inner surface area of the cyclone including lid and the surface of the vortex finder tube and $\lambda_S$ is a friction coefficient which depends on particle loading and has to be predicted experimentally. Again grade efficiency curve for the geometry of a given cyclone is determined from a so called "generalized grade efficiency curve" plotted as a function of the ratio $d_P/d_T$ by similiarity assumption. The shape of the curve is highly dependent on cyclone design and no single curve should be considered generally valid for all cyclones.

This problem, the difficulty in defining $r_i$, the major assumptions made regarding the gas flow field inside the cyclone and the large number of geometrical properties defining the design of a given cyclone constitute major limitations to the usefulness of the static particle approach.

### 2.2.2 Critical Diameter : Timed Flight Approach

This method makes different assumptions about the neglectable forces and accelerations acting on a single particle in the cyclone. An innermost radial position (usually the width or half–width of the cyclone inlet) is assumed for particles entering the cyclone. Particles must travel from this position to the cyclone wall to be collected. The critical particle is the size that travels exactly this distance during its residence time in the cyclone. Different assumptions about initial radial position, the value of the vortex exponent $n$ in equation (1) and residence time lead to different approximate solutions.

E.g. the cut–diameter theory of Lapple [20] assumes an initial radial position for particles at the inlet half–width. If dust is evenly distributed across the inlet opening, particles of the size that travels from the half–width to the wall during the time spent in the cyclone will be collected with 50 % efficiency. The theory gives the following equation for the cut diameter $d_{P,50}$ :

$$d_{P,50} = \sqrt{\frac{9\mu\, b}{2\pi\, \rho_P\, u_i\, N}} \tag{23}$$

The residence time of the particle is determined by $N$, the number of revolutions that the gas stream makes in the cyclone. According to the equation, only one other cyclone dimension, the inlet width $b$, directly affects collection efficiency. For the number of revolutions $N$ an experimentally determined value of $N \approx 5$ is often used. For a given design, increase in cyclone inlet velocity may also increase $N$.

As with the Barth and Muschelknautz theory discussed in 2.2.1 the collection efficiency for a particle of another size can be determined from its ratio to the critical diameter $d_P/d_{P,50}$ and a given "generalized grade efficiency curve". This curve of Lapple has been described by :

$$T(d_P) = \frac{1}{1 + (d_P/d_{P,50})^{-2}} \tag{24}$$

and may not be valid for other cyclone designs.

### 2.2.3 Fractional Efficiency Approach

Other cyclone theories, as e.g. the theory by Leith and Licht [21], have allowed direct calculation of collection efficiency for particles of any size. The model gives a resultant expression for collection efficiency :

$$T(d_P) = 1 - \exp^{-2(C\,\Psi)^{1/(2n+2)}} \tag{25}$$

where n is again the vortex exponent from equation (1). The influences of particle and gas properties are combined in the factor $\Psi$, a modified inertia parameter :

$$\Psi = \frac{\rho_P \, d_P^2 \, u_i \, (n+1)}{18 \mu \, D} \tag{26}$$

with $D$ the diameter of the cylindrical part of the cyclone. The term $C$ is a dimensionless geometry parameter that depends only on the eight cyclone dimension ratios defined by Leith and Licht. For any cyclone design $C$ is constant and a cyclone design with a higher value of the geometry parameter $C$ will lead to higher collection efficiency of the apparatus.

## 2.3 Pressure Drop

Energy costs due to pressure drop represent the major operating expense for cyclone separators. Factors that contribute to pressure drop are :

1. Loss due to expansion or compression of the gas as it enters the cyclone
2. Loss due to wall friction within the cyclone
3. Loss as kinetic energy of rotation in the cyclone vortex
4. Loss due to friction from swirling gas flow in the outlet duct
5. Loss due to contraction of the gas as it enters the outlet duct
6. Recovery of rotational energy as pressure energy in the outlet duct.

Of these factors, rotational energy losses account for the majority of cyclone pressure drop. Different devices have been used to recover rotational energy in the outlet gas stream. But if improperly arranged these devices not only reduce the pressure drop but can also affect or even suppress the vortex within the cyclone. So the use of pressure recovery devices usually results in decreased collection efficiency.

Several expressions have been developed to predict cyclone pressure drop [1, 20, 3, 29, 45, 42, 16]. The expressions from the various models vary greatly in complexity and in the degree to which they rely on empiricism rather than theory. All can be used to calculate the static pressure loss of a cyclone in dependence on geometrical properties and operation conditions of a given cyclone. Due to the huge amount of different expressions in literature and the unsufficient experimental material for there validation the detailed formula of the different approaches has been omitted here.

## 2.4 Conclusions from Theoretical Cyclone Performance Models

As has been pointed out in the former sections gas–particle flows in cyclone separators can be characterized by the following items :

1. The gas–particle flow in cyclones is a real 3–dimensional, complex swirling flow.

2. Flow patterns, operational behaviour and separation performance are influenced by a large number of geometrical properties of the different existing cyclone separator designs as well as by operational conditions (e.g. gas inlet velocity, particle loading).

3. Particle separation is also influenced by the flow history in the inlet configuration, by the design of the dust hopper (e.g. by apex cone) and by measures for pressure loss recovery in the clean gas outlet.

These factors has led to a number of simplifying assumptions which has to be made for theoretical analysis of cyclone flows. Also experimentally proven for the so called standard cyclone designs the resulting cyclone theories can not be applied to other cyclone designs (like e.g. the symmetrical double cyclones described in section 5 without question. But improved standards for the removal of dust from industrial exhaust gases and other industrial requirements can lead to the development of completely revised cyclone designs with further improved performance. Computational fluid dynamics and modern numerical analysis together with the latest findings in high–performance, parallel and cluster computing can make there contribution to the investigation of traditionally used and newly developed cyclone designs. Due to the independence of this kind of analysis from a given geometrical design or given operational conditions the introduction of numerical analysis to the prediction of cyclone performance will lead to greater flexibility and to new cyclone designs with improved particle separation performance.

# 3 Numerical Prediction of Disperse Gas–Particle Flows in Cyclone Separators

## 3.1 Introduction to 3–dimensional Predictions of Cyclone Flows

Also over the last decade computational fluid dynamics has become a widely accepted tool for research and development, the number of publications about experimental investigations of cyclone flows is still far exceeding the number of published numerical investigations. Furthermore a large number of these numerical investigations are still based on 2–dimensional analysis using further assumptions about radial symmetry of the flow in the cyclone which sometimes leads to inadmissible simplifications or can not be applied to some standard cyclone designs used in industrial applications (see also [17]). Only a few publications of the recent years are concerned with an unrestricted 3–dimensional prediction of gas–particle flow in cyclone separators. Results show that the quality of the numerical solution often strongly depends on the used turbulence model for the fluid phase.

Minier [26, 27] uses a 3–dimensional Eulerian–Lagrangian approach on a 3–dimensional numerical grid with approx. 26000 grid cells together with a modified $k$–$\varepsilon$ turbulence model. Also he suggests the use of a Reynolds stress model (RSM), this was prevented by convergence problems. A comparison of the predicted flow field with experimental data is not included in his publications. Minier further uses a Lagrangian model for the prediction of the particulate phase. Variations of the coefficients of restitution in the particle–wall model from elastic to completely inelastic bouncing behavior show only minor influence on the predicted grade efficiency curves.

After a number of 2–dimensional cyclon flow predictions [4, 5] Boysan and Swithenbank present in [6] the theory of a 3–dimensional modified algebraic Reynolds stress turbulence model (ASM). They find a good agreement of the predicted flow field in the investigated cyclone in the range of the potential vortex and an at least qualitative agreement in the core region. For the prediction of the collection efficiency they use a Lagrangian approach together with an eddy-life-time model for turbulence interaction of the particle phase with the fluid. Also the equations for the prediction of particle motion are developed in 3 dimensions it seems from the publication that calculations for the prediction of particle separation were performed only 2–dimensionally (e.g. presented figures of 2–dimensional particle trajectories). Boysan uses different boundary conditions for the particulate phase at different wall regions of the cyclone : total reflection at the lid and the wall of the vortex finder, saltation along the cylindrical wall (particle is replaced in a distance of one grid cell from the wall) and a 100 % collection of the particle if it reaches the conical wall or the entrance to the hopper. The grade efficiency curves predicted from 5000 particle tracks show a fairly good agreement with experimental results of Stairmand [6].

Gorton–Hülgerth [17] and Staudinger [40] performed 3–dimensional predictions for a series of standard cyclones using the commercial computer package FLUENT 4.4.7 and FLUENT UNS 4.2.10 with the build-in RSM turbulence model on a numerical grid with 170000 grid cells. Several different cyclone geometries (e.g. variation of the hopper entrance geometry) has been investigated. Results for the gas velocity field show a very good agreement with the very accurate and detailed LDA measurements of Gorton–Hülgerth [17]. Again the particle flow has been predicted by using only a 2–dimensional Lagrangian approach. Therefore these particle flow predictions could not make any advantage of the accurate fluid flow field predictions because they were carried out on 2–dimensional flow fields calculated with the FLUENT UNS solver. Due to limitations of FLUENT only a simplified model for the particle–wall interaction could be used and only 3500 particle trajectories could be calculated for the prediction of the particle collection efficiency. Nevertheless the predicted grade efficiency curves show a good agreement with experimental data and the semi–empirical model from [45].

Grotjans [48] presents a numerical prediction of a flow in a hydrocyclone using the commercial computer package CFX–5 with two different build-in RSM turbulence models (LRR — Launder, Reece, Rodi closure model; SSG — quadratic Speziale, Sarkor, Gatski closure model). Calculations are carried out on a 3–dimensional hexahedral mesh generated with ICEM/CFD–HEXA with approx. 151000 grid cells. Best agreement with experimental data could be achieved with the SSG formulation of the RSM turbulence model. Predictions of the motion of the particulate phase or the collection efficiency of the investigated cyclone has not been presented in the publication.

Finally Geiger et al. showed in [48] the application of a 3–dimensional large-eddy-simulation model LABFLOW developed by Shell, Netherlands to the numerical prediction of gas–particle flows in FCC cyclone systems. The LABFLOW system is based on the Latice–Boltzman method. A comparison between the measurements and calculations of time averaged tangential velocities at two vertical positions in the cyclone shows excellent agreement between the two. Existing asymmetry around the gas outlet could be observed and was covered by the numerical solution. No attempt was made to calculate the motion of the disperse phase.

Frank et al. [10, 11, 12, 14] developed over the last 5–6 years a 3–dimensional

| $\Phi$ | $S_\Phi$ | $S_\Phi^P$ | $\Gamma_\Phi$ |
|---|---|---|---|
| 1 | 0 | 0 | 0 |
| $u_F$ | $\frac{\partial}{\partial x}\left(\Gamma_\Phi \frac{\partial u_F}{\partial x}\right) + \frac{\partial}{\partial y}\left(\Gamma_\Phi \frac{\partial v_F}{\partial x}\right) + \frac{\partial}{\partial z}\left(\Gamma_\Phi \frac{\partial w_F}{\partial x}\right) - \frac{\partial p}{\partial x} + \rho_F f_x$ | $S_{u_F}^P$ | $\mu_{eff}$ |
| $v_F$ | $\frac{\partial}{\partial x}\left(\Gamma_\Phi \frac{\partial u_F}{\partial y}\right) + \frac{\partial}{\partial y}\left(\Gamma_\Phi \frac{\partial v_F}{\partial y}\right) + \frac{\partial}{\partial z}\left(\Gamma_\Phi \frac{\partial w_F}{\partial y}\right) - \frac{\partial p}{\partial y} + \rho_F f_y$ | $S_{v_F}^P$ | $\mu_{eff}$ |
| $w_F$ | $\frac{\partial}{\partial x}\left(\Gamma_\Phi \frac{\partial u_F}{\partial z}\right) + \frac{\partial}{\partial y}\left(\Gamma_\Phi \frac{\partial v_F}{\partial z}\right) + \frac{\partial}{\partial z}\left(\Gamma_\Phi \frac{\partial w_F}{\partial z}\right) - \frac{\partial p}{\partial z} + \rho_F f_z$ | $S_{w_F}^P$ | $\mu_{eff}$ |
| $k$ | $P_k - \rho_F\, \varepsilon$ | 0 | $\mu + \frac{\mu_t}{\sigma_k}$ |
| $\varepsilon$ | $\frac{\varepsilon}{k}(c_{\varepsilon_1} P_k - c_{\varepsilon_2}\, \rho_F\, \varepsilon)$ | 0 | $\frac{\mu_t}{\sigma_\varepsilon}$ |

$$P_k = \mu_t \left\{ 2 \cdot \left[ \left(\frac{\partial u_F}{\partial x}\right)^2 + \left(\frac{\partial v_F}{\partial y}\right)^2 + \left(\frac{\partial w_F}{\partial z}\right)^2 \right] + \left(\frac{\partial u_F}{\partial y} + \frac{\partial v_F}{\partial x}\right)^2 + \left(\frac{\partial u_F}{\partial z} + \frac{\partial w_F}{\partial x}\right)^2 + \left(\frac{\partial w_F}{\partial y} + \frac{\partial v_F}{\partial z}\right)^2 \right\}$$

$$\mu_{eff} = \mu + \mu_t \quad , \quad \mu_t = \rho_F c_\mu \frac{k^2}{\varepsilon}$$

$$c_\mu = 0.09 \quad , \quad c_{\varepsilon_1} = 1.44 \quad , \quad c_{\varepsilon_2} = 1.92 \quad , \quad \sigma_k = 1.0 \quad , \quad \sigma_\varepsilon = 1.3$$

Table 1: Source terms and transport coefficients for different variables $\Phi$

Eulerian–Lagrangian approach (MISTRAL / PartFlow–3D) for the numerical prediction of 3–dimensional gas–particle flows. Special emphasis was made on parallelization of the numerical algorithm for the prediction of the fluid phase as well as for the 3–dimensional particle trajectory calculation in order to enable numerical preditions for disperse gas–particle flows in large and complex 3–dimensional flow configurations of various industrial applications. The following sections give an outline of the numerical algorithm and the results for its application to two different cyclone separator designs.

## 3.2 The 3–dimensional Eulerian–Lagrangian Approach MISTRAL / PartFlow–3D

### 3.2.1 Basic Equations of Fluid Motion

The following sections deal with an Eulerian–Lagrangian approach for the prediction of 3–dimensional, disperse gas–particle flows and its application for flow simulation in cyclone particle separators. The 3–dimensional, two–phase (gas–particle) flow in cyclone separators is described by assuming that the particulate phase is dilute and that the particle loading is rather low. This assumption satisfies the neglect of inter–particle effects and contributing source terms in the Navier–Stokes equations due to particle–fluid interaction (exchange of momentum between the two phases). Further the two–phase flow is assumed statistically steady, incompressible and isothermal. Then the time–averaged (sometimes called the Reynolds–averaged) form of the governing gas phase equations can be expressed in the form of the general transport equation :

$$\frac{\partial}{\partial x}(\rho_F\, u_F\, \Phi) \;+\; \frac{\partial}{\partial y}(\rho_F\, v_F \Phi) \;+\; \frac{\partial}{\partial z}(\rho_F\, w_F \Phi) \;=\; \frac{\partial}{\partial x}\left(\Gamma_\Phi\, \frac{\partial \Phi}{\partial x}\right) + \frac{\partial}{\partial y}\left(\Gamma_\Phi\, \frac{\partial \Phi}{\partial y}\right) + \frac{\partial}{\partial z}\left(\Gamma_\Phi\, \frac{\partial \Phi}{\partial z}\right) + S_\Phi + S_\Phi^P \quad (27)$$

Here $\Phi$ is a general variable, $\Gamma_\Phi$ a diffusion coefficient, $S_\Phi$ a general source term and $S_\Phi^P$ is the source term due to particle–fluid interaction ($S_\Phi^P \equiv 0$ if momentum coupling of the continous and disperse phase can be neglected). The relationship of $S_\Phi$, $\Gamma_\Phi$, $S_\Phi$ and $S_\Phi^P$ and the constants of the standard k–$\varepsilon$ turbulence model used for the present numerical simulation are given in Table 1.

### 3.2.2 Equations of Motion of the Disperse Phase

The disperse phase is treated by the application of the Lagrangian approach, i.e. discrete particle trajectories are calculated. Each calculated particle represents a large number of physical particles of the same physical properties which is characterized by the particle flow rate $\dot{N}_P$ along each calculated particle trajectory. The prediction of the particle trajectories is carried out by solving the ordinary differential equations for the particle location, translational and rotational velocities. Assuming that the ratio of fluid to particle density is small ($\rho_F/\rho_P \ll 1$) these equations read [9, 44] :

$$\frac{d}{dt}\begin{bmatrix} x_P \\ y_P \\ z_P \end{bmatrix} = \begin{bmatrix} u_P \\ v_P \\ w_P \end{bmatrix} \tag{28}$$

$$\begin{aligned}
\frac{d}{dt}\begin{bmatrix} u_P \\ v_P \\ w_P \end{bmatrix} \;=\; & \frac{3}{4}\frac{\rho_F}{(\rho_P + \frac{1}{2}\rho_F)d_P}\Biggl( v_{rel} C_D(Re_P) \begin{bmatrix} u_F - u_P \\ v_F - v_P \\ w_F - w_P \end{bmatrix} \\
+ \; & \frac{v_{rel}}{\omega_{rel}} C_M(\sigma) \begin{bmatrix} (v_F - v_P)(\omega_z - \Omega_z) - (w_F - w_P)(\omega_y - \Omega_y) \\ (w_F - w_P)(\omega_x - \Omega_x) - (u_F - u_P)(\omega_z - \Omega_z) \\ (u_F - u_P)(\omega_y - \Omega_y) - (v_F - v_P)(\omega_x - \Omega_x) \end{bmatrix} \\
+ \; & \frac{2\nu_F^{1/2}}{\pi|\vec{\Omega}|^{1/2}} C_A \begin{bmatrix} (v_F - v_P)\Omega_z - (w_F - w_P)\Omega_y \\ (w_F - w_P)\Omega_x - (u_F - u_P)\Omega_z \\ (u_F - u_P)\Omega_y - (v_F - v_P)\Omega_x \end{bmatrix}\Biggr) \\
+ \; & \frac{\rho_P - \rho_F}{\rho_P + \frac{1}{2}\rho_F} \begin{bmatrix} g_x \\ g_y \\ g_z \end{bmatrix}
\end{aligned} \tag{29}$$

$$\frac{d}{dt}\begin{bmatrix} \omega_x \\ \omega_y \\ \omega_z \end{bmatrix} = -\frac{15}{16\pi}\frac{\rho_F}{\rho_P}\omega_{rel}\xi_m \begin{bmatrix} \omega_x - \Omega_x \\ \omega_y - \Omega_y \\ \omega_z - \Omega_z \end{bmatrix} \tag{30}$$

with :

$$Re_P = \frac{d_P\, v_{rel}}{\nu} \quad , \quad v_{rel} = \sqrt{(u_F - u_P)^2 + (v_F - v_P)^2 + (w_F - w_P)^2} \quad ,$$

$$\sigma = \frac{1}{2}\frac{d_P\, \omega_{rel}}{v_{rel}} \quad , \quad \xi_m = \xi_m(Re_\omega) \quad , \quad Re_\omega = \frac{1}{4}\frac{d_P^2\, \omega_{rel}}{\nu} \quad ,$$

$$\vec{\Omega} = \text{rot}\ \vec{v}_F \quad , \quad \omega_{rel} = \sqrt{(\omega_x - \Omega_x)^2 + (\omega_y - \Omega_y)^2 + (\omega_z - \Omega_z)^2} \tag{31}$$

These equations of motion of the disperse phase include at the right hand side the drag force, the lift force due to particle rotation (Magnus force), the lift force due to shear in the fluid flow field (Saffman force), the gravitational and added mass forces. For the present numerical investigation the Magnus force due to particle rotation has been neglected because of there minor importance for the very fine particles in the particle diameter range of interest ($d_P < 10\ \mu m$ for a particle density $\rho_P = 2500\ kg/m^3$).

The values for the coefficients $C_D$, $C_M$, $C_A$ and $\xi_m$ and other model constants, e.g. restitution coefficient $k_W$ and coefficient of kinetic friction $f_W$ in the particle–wall collision model can be found in literature [9, 10, 37]. Additionally for the lift coefficient $C_A$ the correction obtained by Mei [24, 37] is taken into account. The effect of fluid turbulence on the motion of the disperse phase, which is regarded to be very important for the particle diameter range under investigation, is modelled by the Lagrangian Stochastic–Deterministic (LSD) turbulence model proposed by Schönung and Milojević [25].

### 3.2.3 Particle–Wall Collision Model

The majority of industrially important disperse multiphase–flows are confined flows, e.g. flows in cyclone seperators or in pneumatic conveying pipe systems. Especially the motion of large particles, which is dominated by inertia, is strongly influenced by the confinement. Considering the wall–collision process it has been shown that irregularities due to wall–roughness and/or deviation of particle shape from sphere play an important role [9, 23, 43].

In this study the particle–wall collisions are treated according to the irregular bouncing model by Sommerfeld [36, 37] in the modified wall roughness formulation given in [44, 9, 10]. The particle collides with an inclined virtual wall (see Fig. 8). The inclination angle $\gamma$ is sampled from a Gaussian distribution with a mean value of 0° and a standard deviation of $\Delta\gamma$. $\Delta\gamma$ depends on the particle diameter $d_P$ and the roughness parameters and may be estimated by:

$$\begin{aligned} \Delta\gamma &= \arctan\frac{2\Delta H_r}{L_r} \qquad \text{for} \quad d_P \geq \frac{L_r}{\sin(\arctan\frac{2H_r}{L_r})} \\ \Delta\gamma &= \arctan\frac{2H_r}{L_r} \qquad \text{for} \quad d_P < \frac{L_r}{\sin(\arctan\frac{2H_r}{L_r})} \end{aligned} \tag{32}$$

Here $L_r$ is the mean cycle of roughness, $H_r$ is the mean roughness height and $\Delta H_r$ is the standard deviation of the roughness height. Since no preferential direction of roughness is assumed, the inclined virtual wall is additionally turned around the normal vector of the original wall by an azimuthal angle $\sigma_a$. This azimuthal angle is sampled from a uniform distribution in the range $[-\pi, \pi]$.

The particle velocities and angular velocities are transformed to a coordinate system that is aligned with the collision plane. For the following equations it is assumed that the $y$–axis of the transformed coordinate system is identical to the normal vector of the collision plane. The computation of the velocities and angular velocities after rebound is carried out by applying the impulse equations and taking into account the sort of collision, i.e. sliding or non–sliding collision [44]:

1. sliding collision for : $\quad -\dfrac{2}{7\, f_W\, (k_W+1)} \;\leq\; \dfrac{v_P^{(1)}}{|v_r|} \;\leq\; 0 \quad :$

$$
\begin{aligned}
u_P^{(2)} &= u_P^{(1)} + \epsilon_x\, f_W\, (k_W+1)\, v_P^{(1)} \quad , \\
v_P^{(2)} &= -\, k_W\, v_P^{(1)} \quad , \\
w_P^{(2)} &= w_P^{(1)} + \epsilon_z\, f_W\, (k_W+1)\, v_P^{(1)} \quad , \\
\omega_x^{(2)} &= \omega_x^{(1)} - \frac{5}{d_P}\, \epsilon_z\, f_W\, (k_W+1)\, v_P^{(1)} \quad , \\
\omega_y^{(2)} &= \omega_y^{(1)} \quad , \\
\omega_z^{(2)} &= \omega_z^{(1)} + \frac{5}{d_P}\, \epsilon_x\, f_W\, (k_W+1)\, v_P^{(1)}
\end{aligned}
\tag{33}
$$

2. non–sliding collision for : $\quad \dfrac{v_P^{(1)}}{|v_r|} \;<\; -\dfrac{2}{7\, f_W\, (k_W+1)} \quad :$

$$
\begin{aligned}
u_P^{(2)} &= \frac{5}{7}\,\Big(u_P^{(1)} - \frac{d_P}{5}\, \omega_z^{(1)}\Big) \quad , \\
v_P^{(2)} &= -\, k_W\, v_P^{(1)} \quad , \\
w_P^{(2)} &= \frac{5}{7}\,\Big(w_P^{(1)} + \frac{d_P}{5}\, \omega_x^{(1)}\Big) \quad , \\
\omega_x^{(2)} &= \frac{2}{d_P}\, w_P^{(1)} \quad , \\
\omega_y^{(2)} &= \omega_y^{(1)} \quad , \\
\omega_z^{(2)} &= -\, \frac{2}{d_P}\, u_P^{(1)}
\end{aligned}
\tag{34}
$$

with :

$$
|v_r| \;=\; \sqrt{\Big(u_P^{(1)} + \frac{d_P}{2}\, \omega_z^{(1)}\Big)^2 + \Big(w_P^{(1)} - \frac{d_P}{2}\, \omega_x^{(1)}\Big)^2}
$$

and :

$$
\epsilon_x \;=\; \frac{u_P^{(1)} + \frac{d_P}{2}\, \omega_z^{(1)}}{|v_r|} \quad , \quad \epsilon_z \;=\; \frac{w_P^{(1)} - \frac{d_P}{2}\, \omega_x^{(1)}}{|v_r|}
$$

In these equations $k_W$ is the coefficient of restitution and $f_W$ is the coefficient of kinetic friction, which can be obtained from literature [9]. The superscripts (1) and (2) indicate values before and after collision, respectively.

### 3.2.4 Solution Algorithm

The time–averaged equations of fluid motion are solved using the program package MISTRAL–3D which is based on a finite volume discretization method on colocated, block–structured numerical grids, developed by Perić and Lilek [33, 34]. The program MISTRAL–3D was extensively modified by the author for gas–particle flow computations. Further modifications involve the implementation of a standard k–$\varepsilon$ turbulence model and the parallelization of the solution algorithm by application of a domain decomposition method. The most fundamental features of MISTRAL–3D are :

- use of non–orthogonal, boundary fitted, numerical grids with arbitrary hexahedral control volumes;
- use of block–structured numerical grids for geometrical approximation of complex flow domains;
- full parallelization using domain decomposition method; parallelization based on standard libraries like e.g. PVM and MPI for maximum portability on high performance computer architectures (e.g. Cray-T3D/T3E, Cray SGI Origin 2000, etc.) and clusters of workstations (e.g. HP, Linux clusters, etc.);
- finite volume solution approach of SIMPLE kind with colocated variable arrangement; Cartesian vector and tensor components;
- full multigrid solution approach for improved convergence of pressure–velocity coupling on large numerical grids.

The solution algorithm for the equations of particle motion is based on the program package PartFlow–3D developed by the research group of the author. Fundamental features of PartFlow–3D are :

- solution of the particles equations of motion for the particle coordinates, translational and rotational velocities by a 4th order Runge–Kutta solving scheme;
- particle tracking on complex, 3–dimensional, block–structured numerical grids;
- taking into account all relevant forces for gas–particle systems with $\rho_F / \rho_P \ll 1$;
- taking into account the effect of fluid turbulence on the motion of the disperse phase by a Lagrangian Stochastic–Deterministic (LSD) turbulence model;
- particle–wall collision model including a particle diameter dependend wall roughness model;

- capability for the prediction of higher concentration effects by taking into account two–way coupling in particle–fluid momentum interaction and particle–particle collisions;
- prediction of mean particle properties, e.g. mean translational and rotational velocities and theire r.m.s. values, volume or mass concentration, particle number density, mean particle diameter, etc.;
- calculation of particle erosion intensity on solid boundaries of the flow domain;
- full parallelization using either static or dynamic domain decomposition for optimum work load balancing and maximum parallel efficiency.

A more detailed description of the 3–dimensional solution algorithm and the developed parallelization methods for the Lagrangian approache can be found in [10, 11, 13].

# 4 Numerical Prediction of Gas–Particle Flow in a Standard Cyclone

The presented 3–dimensional Eulerian–Lagrangian approach was applied to the gas–particle flow in a standard cyclone (Fig. 9). The calculations were based on experimental investigations carried out by König [19] on a series of geometrically similiar cyclones for a number of different inlet gas velocities.

## 4.1 Flow Geometry and the Numerical Grid

The cyclones Z10, Z20, Z40 and Z80 investigated in this paper were determined by the following geometrical properties (see also Fig. 9) :

| | | Z10 | Z20 |
|---|---|---|---|
| Diameter of the cyclon | $D$ | 40 $mm$ | 80 $mm$ |
| Height of the cyclon | $H$ | 195 $mm$ | 390 $mm$ |
| Inlet cross section | $a \times b$ | $4.5 \times 18$ $mm^2$ | $9 \times 36$ $mm^2$ |
| Diameter of the gas exit | $d_T$ | 10 $mm$ | 20 $mm$ |
| Height of the gas exit | $h_T$ | 31 $mm$ | 62 $mm$ |
| Diameter of the particle exit | $d_B$ | 10 $mm$ | 20 $mm$ |
| | | Z30 | Z40 |
| Diameter of the cyclon | $D$ | 160 $mm$ | 320 $mm$ |
| Height of the cyclon | $H$ | 780 $mm$ | 1560 $mm$ |
| Inlet cross section | $a \times b$ | $18 \times 72$ $mm^2$ | $36 \times 144$ $mm^2$ |
| Diameter of the gas exit | $d_T$ | 40 $mm$ | 80 $mm$ |
| Height of the gas exit | $h_T$ | 124 $mm$ | 248 $mm$ |
| Diameter of the particle exit | $d_B$ | 40 $mm$ | 80 $mm$ |

Due to the complex geometry of the cyclone a numerical grid with 42 different grid blocks and about 250.000 finite volume elements had to be designed for a first series of numerical calculations of the gas–particle flow (Fig. 10.a). In a second numerical investigation the numerical grid was redesigned using the grid generator ICEM/CFD–HEXA and taking into account the apex cone and the particle collecting hopper (72 grid blocks, about 350.000 finite volume elements, see Fig. 10.b). The numerical grid was originally designed for the Z10 cyclone and then proportionally scaled as 1 : 2 : 4 : 8 for the other three cyclones Z20–Z80.

## 4.2 Prediction of the Gas and Particle Flow, Pressure Loss

In the course of first calculations of the gas flow field in the cyclones it was found that the numerical mesh needed further improvement and certain grid refinement in regions of large fluid velocity gradients in order to get converged solutions. Grid refinement was applied to the gas inlet and to the region in the vicinity of the lower end of the gas exit tube. But certain restrictions in the mesh generation algorithm of CFX 4.2C prevented an optimum arrangement and design of the finite volume elements in some regions of the flow geometry. Consequently strong underrelaxation had to be applied for the solution algorithm in order to obtain convergence, mainly due to the convergence behavior of the $k$–$\varepsilon$ equations.

Unfortunately there is no experimental data material about the velocity fields in the Z10,. . .,Z80 cyclones in the publication of König. But the flow in cyclone separators was studied in the past by many authors and thus the calculated flow field can be assessed at least qualitatively. Fig. 11.a) and 11.b) show the distribution of the mean gas velocity and the fluid pressure respectively in two perpendicular cross sections of the Z10 cyclone. The calculated flow field in Fig. 11.a) shows the typical asymmetrical main vortex in the upper cylindrical section of the cyclon, the core structure of the velocity field and the strong acceleration of the fluid in the region below the clean gas exit. This corresponds to the radial pressure distribution in the main body of the cyclone and to the region of main pressure drop near the clean gas exit in Fig. 11.b). In a more detailed view (see Fig. 12 — 15 typical recirculating flow can be found along the lid of the cylindrical part of the cyclone and further downwards along the outer wall of the vortex finder tube. This kind of recirculating flow is well known for cyclone separators from literature. The flow field in the other parts of the cyclone is also in qualitative agreement with the knowledge available for the flow in cyclone separators.

So Figs. 12 — 15 show the strong secondary flow along the conical walls of the cyclone downwards to the entry cross section of the particle collecting hopper. On Figs. 14 and 15 it can be observed that a certain amount of gas volume flow rate is entering the hopper and leads to complex 3–dimensional recirculating flows in the particle hopper volume. The gas flow is then recirculating along the surface of the apex cone back into the main body of the cyclone where it forms the upward flowing vortex core. It can clearly be seen from Figs. 14 and 15 that the vortex core is slightly oscillating around the cyclone vertical axis. All the Figs. 12 — 15 show the strong asymmetry of the fluid flow in the cyclone which can not be predicted by simplified 2–dimensional simulations.

For further comparison the pressure loss over the cyclone was predicted for various gas inlet velocities and compared with the experimental data of König (Fig. 17). The pressure loss data of König take only into account the difference of the static pressure before and after the cyclone. The diagram shows an underprediction of the pressure loss obtained from the numerical calculations for all investigated gas inlet velocities. The reason for that is most likely to be found in differences between the experimental setup for the locations of pressure measurements and the flow geometry investigated numerically. The numerical data of the pressure loss show a comparable increase with increasing gas inlet velocity.

Particle trajectory calculations were carried out using the described Lagrangian approach with the predicted gas flow fields in order to obtain particle separation rates for the four different cyclones (see Fig. 18 — 21). Main difficulties in the calculation of particle motion could be observed in the following :

1. The flow in the cyclone leads to a very large number of particle–wall collisions. The detection of a particle–wall collision results in a decrease of the integration time step of the solution algorithm. Therefore the large number of particle–wall collisions lead to large computation time for the prediction of the particle motion.
2. The large computation time needed for cyclone flow prediction is also determined by consideration of the influence of gas flow turbulence on particle motion. In order to ensure accuracy the integration time step is set to be less then 1/10 of the turbulent time scale of the LSD turbulence model. The resulting small time steps of the Runge–Kutta solver for the particle equations of motion contribute to the large computational effort needed for the present simulation.
3. The larger geometrical size of the Z40 and Z80 cyclones lead to a substantial increase of particle residence time in the cyclone and thus to larger computation time.

As a result the calculation of about 10.000 particle trajectories in the cyclon separator takes about 22 hours of CPU–time on a single MIPS R10000 processor of a Silicon Graphics CRAY Origin 2000. Fig. 16 shows representative examples of particle trajectories in the Z10 cyclone with an inlet gas velocity of $u_F = 10\ m/s$. The numerical predicted particle cut–off diameter for particles with $\rho_P = 2500\ kg/m^3$ is about $d_{P,50} = 2.0\ \mu m$. In accordance with that Fig. 16.a) shows a significant smaller particle which is captured by the secondary flow along the cyclone lid and follows that secondary flow directly along the wall of the vortex finder tube to the clean gas exit. In the case of Fig. 16.b) a particle with $d_P = 2.02\ \mu m$ is first of all moving along the outer conical wall to the particle hopper. But due to its small size it can not be collected there. It follows the recirculating gas flow back into the cyclone main body where it is separated again. After a second cycle through the particle hopper the small particle is now captured into vortex core and moves straight upward to the clean gas exit.

A slightly larger particle in Fig. 16.c) is first of all captured in a particle rope along the cyclone lid. But it is too large in order to follow the recirculating flow to the vortex finder tube inlet cross section. After certain time of recirculation this particle can be separated and moves fairly straight down to the particle hopper where it is collected. Fig. 16.d) shows typical particle behavior of particles with diameters $d_P \gg d_{P,50}$. These larger particles are clearly separated by the main vortex flow due to centrifugal forces and can be collected in the particle hopper after short residence times in the cyclon main body.

Besides the characteristic flow patterns for particle trajectories of different particle size Fig. 16.a) – d) show furthermore a disadvantage of the cyclone design investigated by König in [19]. Due to the design of the tangential gas inlet configuration with a vertical offset against the lid of the cyclone particles tend to formation of a strong particle rope in the cylindrical region above the inlet. Large particle residence times in that region lead to large particle concentrations and a high particle erosion intensity along the walls near that rope. Also not observed in the numerical simulations (due to limitations of the mathematical models used in the Lagrangian approach) it is reported from experiments that this particle behavior can lead to a critical accumulation of particles in the rope and a periodical break-down of this rope. This leads to observable pressure fluctuations and unsteady flow regime in the cyclone connected with a substantial decrease in cyclone performance.

Another rope formation can be observed by looking at the plot of particle erosion intensity on the conical walls of the cyclone as shown in Fig. 23. It can clearly be seen from the Fig. 23, that particles are following a spiral path along the cyclone walls on theire way from the gas inlet to the particle collecting hopper. This spiral rope has been often observed in experimental investigations and could be reproduced the first time in the present numerical simulations.

## 4.3 Calculation of the Particle Collection Efficiency

In accordance with the experiments of König [19] the investigations for the prediction of the particle collection efficiency were carried out for the physical properties of a fraction of quartz particles of the Busch company. The original quartz dust had a particle diameter distribution in the range of $d_P = 0 \dots 50\ \mu m$ with a mean particle diameter of $\overline{d_P} = 10.9\ \mu m$. The numerical simulations were carried out for 20 particle diameter classes in the range between $0.5 \dots 15\ \mu m$. A total number of 670 particle trajectories with random initial conditions in the inlet cross section were calculated for each of the 20 particle diameter classes. Even not stated in the publication of König a particle density of $\rho_P = 2500\ kg/m^3$ was assumed for the quartz particles. For the coefficients of restitution and kinetic friction typical values for quartz particles were used ($k_W = 0.8$, $f_W = 0.35$).

In a first series of calculations the separation rates for the quartz particles were predicted for all four cyclones Z10,. . .,Z80 with an inlet gas velocity of $u_F = 10\ m/s$. Then the separation rate can be predicted as :

$$T(d_P) = 1 - \frac{\dot{N}_{out}(d_P)}{\dot{N}_{in}(d_P)} \tag{35}$$

where $\dot{N}_{in}(d_P)$ and $\dot{N}_{out}(d_P)$ are the particle flow rates for a given particle size in the inlet cross section and gas exit cross section respectively. In the numerical prediction particles are assumed to be collected in the cyclone, if :

1. The particle trajectory reaches the inlet cross section of the particle hopper.
2. The particle sticks to the wall of the cyclone (that means the wall normal velocity of the particle after a particle–wall collision is less than $10^{-5}\ m/s$).
3. The particle residence time in the cyclone is larger than the maximum allowed computation time, which was set to $T_{max} = 150\ s$ for Z10, Z20 and to $T_{max} = 250\ s$ for cyclones Z40, Z80 due to there larger geometrical size. The value for $T_{max}$ was choosen in a way, that the number of particles with this very large residence time in the cyclone was less than 4–5 % of the calculated particle trajectories.

Fig. 18–21 show the comparison of the numerically predicted particle separation rates with the experimental results of König. The figures show for all four different cyclones a very good agreement of the numerical and experimental results. The shape of the grade efficiency curves is nearly identical, even if for the smaller cyclones Z10 and Z20 a slight shift of the grade efficiency curve towards higher particle diameters can be observed. For the Z40 and Z80 cyclones actually no difference between the numerical and experimental results can be found. The small difference for Z10 and Z20 can be explained by the larger influence of the inner vortex core on the particle separation in the Z10 and Z20 cyclones due to theire smaller geometrical dimensions. The $k$–$\varepsilon$ turbulence model used in the present simulations gives larger deviations within that region in comparison with an experimentally predicted flow field. For the larger cyclones Z40 and Z80 this errors in the predicted gas flow fields are of minor importance for the particle separation process and lead therefore to a better agreement of the predicted cyclone performance with experimental data.

In a second step the gas inlet velocity for the Z20 cyclone was varied. Fig. 22 shows the results for the two gas inlet velocities $u_F = 4.3\ m/s$ and $u_F = 10\ m/s$. Again the experimentally and numerically predicted separation rates are in very good agreement. Furthermore the numerical simulation gives the right tendency of a shift of the cut–off particle diameter towards larger particles for decreased gas inlet velocities. This result could also be established in numerical simulations for the other cyclones with varied gas inlet velocity.

# 5 Prediction of Particle Separation in Symmetrical Double Cyclone Separators

In further investigations the 3–dimensional Eulerian–Lagrangian approach MISTRAL/PartFlow–3D was applied to the gas–particle flow in two different types of symmetrical double cyclone separators (Fig. 27 and Fig. 28) developed by Schneider at LUT GmbH, Eckernförde (see publications in [2, 50, 35]). Based on former work of Feifel [8] Schneider et al. developed a number of efficient symmetrical double cyclone separators which are able to change the opinions about the limits in operation of cyclone technology. These cyclone developments are based on new findings and investigations on details of the cyclone flow, e.g. about the secondary flows and their effects on particle separation as well as about the mechanisms of particle discharge from the separation chambers of the cyclones to the settling chambers and particle hoppers. From these latest investigations it was found that the secondary flows of a swirling flow like in cyclone separators can be determindely used for an improvement of particle separation efficiency.

The symmetrical double cyclone has been investigated as experimentally by Schneider et al. as well as numerically by Frank et al. The central goal of the investigations was a gain in knowledge about the complex vortex flow in the cyclone, about particle motion and separation efficiency of this special types of symmetrical double cyclone separators. In accordance with the first experimental results such cyclones are able to operate with a cut–off particle diameter of $x_{ae,50} = 50, \ldots, 500\ nm$. These values for the cut–off particle diameter in the submicron range has been measured for cyclone geometries with diameters of the separation chamber of 40 to 230 $mm$ and for circumferential gas velocities in the separation chamber of about $u_F = 10, \ldots, 25\ m/s$. The given particle diameter

$$x_{ae} = d_P \sqrt{\rho_P / \rho_{P0}} \tag{36}$$

with $\rho_{P0} = 1000\ kg/m^3$ is the so called "aerodynamical" particle diameter commonly used for comparison in aerosol technology and corresponds to a particle to fluid density ratio of $\rho_P/\rho_F = 1000\ kg/m^3$.

| | | ZS18 / ZS30 | ZT30 |
|---|---|---|---|
| 1. Diameter of the cyclon at symmetry plane | $D_1$ | 230 mm | 230 mm |
| 2. Diameter of the cyclon at the entrance of the settling chamber | $D_2$ | 120 mm | 120 mm |
| 3. Length of the conical cyclon main section | $L_K$ | 253 mm | 253 mm |
| 4. Length of the cylindrical cyclone section | $L_Z$ | 100 mm | 400 mm |
| 5. Diameter of the clean gas exit | $D_T$ | 70 mm | 70 mm |
| 6. Distance of the clean gas exit from the symmetry plane | $L_T$ | 15 mm | 15 mm |
| 7. Inlet cross section | $B \times H$ | $100 \times 82\,\mathrm{mm}^2$ | $320 \times 20\,\mathrm{mm}^2$ |
| 8. Size of particle settling chamber | $B_b \times H_b \times T_b$ | $80 \times 538 \times 276\,\mathrm{mm}^3$ | $80 \times 538 \times 276\,\mathrm{mm}^3$ |

Table 2: Geometrical parameters for the investigated symmetrical double cyclone separators ZS and ZT.

## 5.1 Flow Geometry and General Flow Patterns

Numerical investigations were based on two different types of symmetrical double cyclone separators which are both result of the cyclone development of Schneider et al. mentioned above. These two different cyclone designs differ mostly in the design of the inlet of particle laden gas flow into the cyclon separation chamber. Fig. 24 shows such a symmetrical double cyclone separator with spiral inflow (ZS).

The double cyclon has a rotational symmetric separation chamber (**3**, Fig. 24) which is also symmetrical in relation to the center plane (**Z**) between the two conical parts of the separation chamber. The gas–particle flow enters the cyclone by a spiral (**2**, Fig. 24) or tangential (**1**, Fig. 25) inflow channel leading to a strong swirling flow and formation of a steady primary vortex (**2**, Fig. 26) in the separation chamber. The swirling flow produces a centrifugal force acting on the particles which causes radial movement of the solid particles towards the wall of the separation chamber. Further, in the conical parts of the cyclone separation chamber two secondary ring vortices (**3**, Fig. 26) of toroidal shape are induced by the radial pressure gradient of the primary vortex. Particles are moved by these secondary vortices to the entrance of the particle hopper (**4**, Fig. 26) which are formed by the circular edges of the outer casing of the conical separation chamber (**3**, Fig. 24) and by the deflector cone (**4**, Fig. 24) attached to the outer walls of the vortex finder tubes (**6**, Fig. 24). Particles are moved through these circular slits into the sedimentation chambers (**5**, Fig. 26) by the secondary flow. The continuous phase cleaned from solid particles recirculates along the outer wall of the vortex finder tubes to the clean gas exit and leaves the cyclone through both the vortex finder tubes (**6**, Fig. 26).

Therefore the separation of solid particles from a gas–particle dispersion in the double cyclone separator consists of two stages : 1. the separation of the solid particles from the continuous phase by radial movement of particles and particle agglomerates by centrifugal forces in the separation chamber, and 2. the discharge of particles and particle agglomerates from the separation chamber and further agglomeration and gravitational sedimentation in the flow region of the sedimentation chamber and particle hopper.

The geometrical parameters for both investigated symmetrical double cyclone separators are given in Table 2. For the cyclone with spiral inflow configuration (ZS) additionally two different positions of the apex cone (**4**, Fig. 24) has been investigated. The apex cone is a flow guiding equipment which is attached at the lower end of the conical part of the cyclone separation chamber to the outer diameter of the vortex finder tubes. The gap width between the apex cone and the cyclone wall was varried from $h_{ac} = 18.7\ mm$ (ZS18) to $h_{ac} = 30.0\ mm$ (ZS30). In a further investigation numerical predictions were performed for a symmetrical double cyclone separator with tangential inflow configuration shown in Fig. 25. In order to ensure the same gas inlet velocity for comparable volume flow rates of particle laden gas for both types of cyclones ZS and ZT the cylindrical part of the separation chamber (**3**, Fig. 25) had to lengthend for ZT30. The gap width between the apex cone and the cyclone wall was choosen $h_{ac} = 30.0\ mm$ for the ZT cyclone.

## 5.2 Operating Conditions

For all numerical investigations a constant gas inlet velocity of $u_{F,in} = 25.0\ m/s$ with a turbulence intensity of 10 % was assumed. For the particle phase calcium carbonate (limestone) particles were used in the experimental investigations of Schneider et al. [35]. The used limestone powder is produced under the trading name OMYACARB 2–GU by OMYA GmbH, Köln/Germany. The particle material is characterized by a particle density of $\rho_P = 2700\ kg/m^3$ and a carbonate content in the raw material of more than 98 %. The medean value of the particle size distribution sum $Q_3(x)$ for the used material is $x_{50,3} = 2.5\ \mu m$. In the experiments the particle concentration in the raw gas flow was $0.1, \ldots, 0.8\ kg/m^3$ which corresponds to operating conditions of these types of cyclones in environmental technology. The low particle concentration values satisfy the assumption of the so called one–way coupling between the fluid and particle phase in the numerical simulations.

Unfortunately there were no exact values for the parameters of the particle–wall collision model of the numerical approach. So we used data for similiar particle/wall material combinations from literature. Values for the coefficient of restitution $k_W = 0.5$ and for the coefficient of kinetic friction $f_W = 0.45$ were used for the numerical simulations which corresponds to the combination of limestone particles and a steel wall. The small particle diameters lead to a dominant influence of the aerodynamic forces and very short particle relaxation times after particle–wall interactions. Therefore we dont expect a great influence of these particle–wall collision model parameters on the predicted cyclone separation performance.

## 5.3 The Numerical Grids for ZS and ZT Cyclones

In contrast to most of the investigations for the standard cyclones presented in section 4 for the numerical predictions of gas–particle flow in the symmetrical double cyclone separators the flow region around the apex cone as well as the particle hopper have been taken into account. Due to the complex flow geometry of the investigated cyclone separators numerical grids with up to 95 different grid blocks and about 350.000 grid cells had to be designed for the numerical calculations of the gas–particle flow (see Figs. 27 and 28). Also the numerical effort is substantially increased, the calculated gas flow fields give the opportunity to study the process of particle separation and particle removal from the cyclon separation chamber to the particle hopper by secondary flows in greater detail.

## 5.4 Results of the Numerical Predictions and Comparison with Experimental Data

### 5.4.1 The Flow Field of the Fluid Phase

The numerical flow simulations confirm the expected main vortex flow structure known from cyclone theory and from experimental observations. The flow field in the two perpendicular cross sections shown in Fig. 29 and Fig. 31 clearly show the secondary flow from the spiral inlet to the cyclone along the wall of the conical part of the separation chamber towards the inlet cross section of the settling chamber with the attached apex cone. Along the outer wall of the vortex finder tube the gas flow reaches the inlet cross section of the vortex finder tube near the symmetry plane and further exits the cyclone through the clean gas exit. Fig. 30 and Fig. 32 especially show, that there is a secondary flow from the conical separation chamber through the gap at the apex cone into the settling chamber. This secondary flow is led to the walls of the particle sedimentation chamber by the guiding equipment attached to the outer diameter of the vortex finder tubes and allows also for smaller particles to agglomerate and to sedimentate as larger agglomerates in the sedimentation chamber. Therefore this recirculating flow was found to be of particular importance for the process of particle separation in the cyclone separator (see also Figs. 33 and 34).

### 5.4.2 Prediction of Particle Separation

Further numerical investigations were focused on the prediction of the particle separation for the cyclone geometries ZS18, ZS30 and ZT30 from particle trajectory calculations. Numerical simulations were carried out for 20 particle diameter classes in the range between $0.5 \ldots 15\ \mu m$. A total number of 670 particle trajectories with random initial conditions in the inlet cross section were calculated for each of the 20 particle diameter classes.

Figs. 33 and 34 show some examples of particle trajectories in the ZS18 and ZT30 cyclones for particles with $d_P = 0.5, \ldots, 6.0\ \mu m$. Besides the main features of particle behavior allready discussed in section 4.2 for the particle tracks in the standard cyclone Fig. 33 shows a further disadvantage of the cyclone design with a spiral inflow configuration. So for particle trajectories with $d_P > d_{P,50}$ it could be observed that such larger particles spend a significant amount of theire residence time in the spiral inflow segment. Due to centrifugal forces these particles are moving in a small distance to the cyclone walls and are hindered by the "step" between the inflow spiral and the conical part of the cyclone to follow the secondary flow towards the entrance to the particle hopper. Besides larger particle residence times and a decreased cyclone performance this particle behavior could lead to particle erosion problems at the side walls of the inflow spiral in the case of highly abrasive particle material.

For the prediction of particle separation efficiency $T(d_P)$ can be predicted again in accordance with equation (35). For the numerical predictions the following particle collection criterion has been assumed :

1. The particle sticks to the wall of the cyclone (that means the wall normal velocity of the particle after a particle–wall collision is less than $10^{-5}\ m/s$).

2. The particle trajectory reaches the particle settling chamber and exceeds a given maximum residence time inside the cyclone. For the present simulations this time was set to $T_{P,max} = 120\,\mathrm{s}$.

Figs. 35.a) —35.c) show the comparison of the numerically predicted particle separation rates with the experimental results of Schneider et al. [35, 2, 50] for limestone particles with $\rho_P = 2700\ kg/m^3$. Additionally the numerical results for particle separation for $\rho_P = 1000\ kg/m^3$ are given in the diagrams (which correspond to the so called "aerodynamic" particle diameter). Figures show a shift of the particle separation rates and the $d_{P,50}$ particle diameter ($T(d_{P,50}) = 0.5$) towards higher particle diameters (for about 2 $\mu m$) for the numerical predictions. Nevertheless, under consideration of all uncertainties involved in both the experimental and numerical investigations this has to be regarded as a fairly good agreement. Basically there are three main reasons for the differences in the numerically predicted particle separation rate results :

1. Certainly the complex fluid flow field in the cyclone could not be covered in all quantitative details by the present numerical simulations. Coarse numerical grid resolution in some regions of the flow domain and the used k–$\varepsilon$ turbulence model cause some quantitative errors in the fluid flow calculations.

2. The Lagrangian approach used for the prediction of the particle motion does not yet account for the particle agglomeration which seems to be important for the exact prediction of particle separation in this special type of symmetrical double cyclone separators.

3. It seems that collection of small particles with $d_P \leq 1.0\ \mu m$ is not only influenced by agglomeration but also by adhesive and electrostatic forces contributing to the observed difference in the obtained numerical results in Figs. 35.a) —35.c).

Implementation and use of a Reynolds stress turbulence model, improvement of the numerical grid, especially in the region near the apex cone which is important for particle separation processes, together with the development of a particle–particle agglomeration model can substantially improve the numerical results for the prediction of particle separation in cyclone separators.

### 5.4.3 Particle Concentration Distribution and Particle Erosion

The supposition of an influence of agglomeration processes on the separation performance of the investigated cyclones is supported by observations of rope formation from the numerical predictions for the ZT30 cyclone. First of all a ring shaped particle rope can be observed in the vicinity of the symmetry plane. This particle rope is caused by the weak secondary flow in that region and the therefore low axial particle transport in connection with the steady particle inflow rate from the inlet cross section. Furthermore Fig. 36 shows a spiral particle rope separating from the edge of the tangential inflow of ZT30. This particle rope can be observed in both the particle erosion pattern on the wall of the symmetrical double cyclone (Fig. 36) and in the distribution of the relative particle number flow rate (Fig. 37).

Fig. 37 shows also the high particle concentration in the particle settling chamber which can exceed the particle concentration in the inlet by more than a factor of 10. This high particle concentrations are caused by large particle residence times of particles with $d_P \simeq d_{P,50}$ within the cyclone separation chamber and the particle hopper. Both effects can contribute to the formation of particle agglomerates which are subject to forced particle separation and collection due to theire higher inertia and therefore contribute to an improved overall cyclone performance.

# 6 Conclusions

The paper gives an overview of the state–of–the–art knowledge about the flow of particle laden gas in cyclone separators. In a short outline existing theoretical and semi–empirical models for the prediction of particle separation efficiency in cyclones are summarized.

Furthermore the paper gives the formulation of a 3–dimensional Eulerian–Lagrangian approach for the numerical prediction of disperse gas–particle flows. The numerical approach has been applied to the gas–particle flow in a series of geometrically similiar standard cyclones as well as to the flow in two different designs of so called symmetrical double cyclone separators. Inlet conditions and the position of the apex cone near the entrance of the particle settling chamber has been variied in the numerical predictions. Results for the gas flow field, the particle trajectories, the particle separation efficiency and mean particle properties have been presented. The comparison of the numerical results with existing experimental data of König [19] and Schneider et al. [35, 2, 50] show a good agreement for the predicted cyclone performance and the applicability of the numerical approach to complex 3–dimensional disperse gas–particle flows. The effect of higher particle concentrations and particle agglomeration on the particle separation process in cyclones need further investigation.

# 7 Acknoledgement

The author thanks Prof. M. Perić for the provision of his laminar CFD code FAN–3D for this research, which formed the starting point for the development of the presented numerical approach MISTRAL/PartFlow–3D. Further this work was supported by the Deutsche Forschungsgemeinschaft (DFG) under Contract No. SFB 393/D2.

# References

[1] Alexander R. McK. : "Fundamentals of Cyclone Design and Operation", Proc. Australas. Inst. Min. Metall. (New Series), pp. 152–153, 203 (1949).

[2] Bachmann Ch., Schulz U. : "Experimentelle Ermittlung der Abscheideleistung von Hochleistungsentstaubern für feste Partikeln aus Gasen — Effektivität und Wirtschaftlichkeit", Diploma thesis, Flensburg University of Applied Sciences, (1996).

[3] Barth W. : "Berechnung und Auslegung von Zyklonabscheidern aufgrund neuer Untersuchungen", Brennstoff+Wärme+Kraft, 8, Nr. 1, pp. 1–9, (1956).

[4] Boysan F., Ayers W.H., Swithenbank J. : "A Fundamental Mathematical Modelling Approach to Cyclone Design", Trans IChemE, Vol. 60, pp. 222–230, (1982).

[5] Boysan F., Ewan B., Swithenbank J., Ayers W.H. : "Experimental and Theoretical Studies of Cyclone Separator Aerodynamics", I. Chem. E. Symposium Series No. 69, pp. 305–319, (1983).

[6] Boysan F., Swithenbank J., Ayers W.H. : "Mathematical Modelling of Gas–Particle Flows in Cyclone Separators", Encyclopedia of Fluid Mechanics, Vol.4 Solids and Gas–Solids Flows, Chapter 42, Gulf Publishing Company, Houston, Texas (1986).

[7] Cheremisinoff N.P., Cheremisinoff P.N. : "Particle Capture from Process Gas Streams", Encyclopedia of Fluid Mechanics, Vol.4 Solids and Gas–Solids Flows, Chapter 40, Gulf Publishing Company, Houston, Texas (1986).

[8] Feifel E. : "Zyklonentstaubung, Neuere Anschauungen und Ergebnisse", Mitteilungen des VGB, Vol. 92, pp. 52–57, (1943).

[9] Frank Th. : "Numerische Simulation der feststoffbeladenen Gasströmung im horizontalen Kanal unter Berücksichtigung von Wandrauhigkeiten", PhD Thesis, Techn. University Bergakademie Freiberg, Germany, (1992).

[10] Frank Th., Wassen E., Q. Yu : "A 3–dimensional Lagrangian Solver for Disperse Multiphase Flows on Arbitrary, Geometricaly Complex Flow Domains using Block–structured Numerical Grids", 7th Int. Symposium on Gas–Particle Flows, ASME Fluids Engineering Division Summer Meeting, Vancouver, BC, Canada, June 22–26, 1997, CD–ROM Proceedings, FEDSM97–3590, (1997).

[11] Frank Th., Wassen E. : "Parallel Efficiency of PVM– and MPI–Implementations of two Algorithms for the Lagrangian Prediction of Disperse Multiphase Flows", JSME Centennial Grand Congress 1997, ISAC '97 Conference on Advanced Computing on Multiphase Flow, Tokyo, Japan, July 18–19, 1997.

[12] Frank Th., Wassen E., Yu Q. : "Lagrangian prediction of disperse gas–particle flow in cyclone separators", ICMF '98 — 3rd International Conference on Multiphase Flow 1998, Lyon, France, June 8.–12., 1998, CD–ROM Proceedings, Paper No. 217, pp. 1–8.

[13] Frank Th., Wassen E., Yu Q. : "Effiziente parallele Algorithmen für die numerische Simulation 3–dimensionaler, stark phasengekoppelter, disperser Mehrphasenströmungen", Zwischenbericht zum DFG–Sonderforschungsbereich 393, Teilprojekt D2, TU Chemnitz, FG Mehrphasenströmungen, Chemnitz, Germany, June 1998.

[14] Frank Th., Schneider J., Yu Q., Wassen E. : "Experimental and Numerical Investigation of Particle Separation in a Symmetrical Double Cyclone Separator", 8th Int. Symposium on Gas–Particle Flows, ASME Fluids Engineering Division Summer Meeting, San Francisco, CA, U.S.A., July 18–22, 1999.
CD–ROM Proceedings, Paper No. FEDSM99–7865, pp. 1–10, (1999).

[15] Frank Th., Schneider J., Bernert K. : "Numerische Untersuchung der Gas–Partikel–Strömung in symmetrischen Doppelzyklonabscheidern", VDI–Berichte 1511, VDI–Verlag Düsseldorf, pp. 197–214, (1999).

[16] Greif V. : "Reduzierung des Druckverlustes von Zyklonabscheidern durch Rückgewinnung der Drallenergie sowie Abscheidung bei kleinen und kleinsten Staubbeladungen", VDI–Fortschritts–Berichte, Reihe 3 : Verfahrenstchnik, Nr. 470, VDI–Verlag Düsseldorf, (1997).

[17] Gorton–Hülgerth A. : "Messung und Berechnung der Geschwindigkeitsfelder und Partikelbahn im Gaszyklon", VDI–Fortschritt–Bericht, Reihe 7, Nr. 357, (1999).

[18] Kirch R. : "Der Einfluß der Turbulenz auf die Partikelbewegung im Gaszyklon", VDI–Fortschritts–Berichte, Reihe 7 : Strömungstechnik, Nr. 145 (1988), VDI–Verlag Düsseldorf.

[19] König C. : "Untersuchungen zum Abscheideverhalten von geometrisch ähnlichen Zyklonen", PhD Thesis, University of Kaiserslautern, Germany, (1990).

[20] Lapple C.E. : "Gravity and Centrifugal Separation", Ind. Hyg. Quart., 11:40 (1950).

[21] Leith D., Licht W. : "The Collection Efficiency of Cyclone Type Particle Collectors — A New Theortical Approach", A.I.Ch.E. Symp. Series, 68:196 (1972).

[22] Löffler F. : "Staubabscheiden", Thieme Verlag, Stuttgart, New York (1988).

[23] Matsumoto S., Saito S., Maeda S. : "Simulation of gas–solid two–phase flow in horizontal pipe", Journal of Chemical Engineering of Japan, Vol. 9, No. 1, pp. 23–28, (1976).

[24] Mei R. : "An approximate expression for the shear lift force on a spherical particle at finite Reynolds number", Int. J. Multiphase Flow, Vol. 18, pp. 145–147, (1992).

[25] Milojević, D. : "Lagrangian Stochastic–Deterministic (LSD) Predictions of Particle Dispersion in Turbulence", Part. Part. Syst. Charact., Vol. 7, pp. 181–190, (1990).

[26] Minier J., Simonin O., Gabillard M. : "Numerical Modelling of Cyclone Separators", Int. Conf. on Fluidized Bed Combustion, (1991).

[27] Minier J., Simonin O. : "A Numericalal Approach of Cyclone Separators", 2nd European SYMP, Separation of Particles from Gases, March 1992, pp. 121–136.

[28] Patent DRP 39219, Knickerbocker Company, Jackson, USA, (1886).

[29] Muschelknautz E. : "Die Berechnung von Zyklonabscheidern für Gase", Chem.–Ing.–Technik 44, Nr. 1+2, pp. 63–72, (1972).

[30] Muschelknautz E. : vt-Hochschulkurs II Mechanische Verfahrenstechnik, Teil 1: Verfahrenstechnik vt 3 (1972); Teil 2 : vt 5 (1972); Teil 3 : vt 9 (1972); Teil 4 : vt 10 (1972); Teil 5 : vt 6 (1973); Teil 6 : vt 8 (1974).

[31] Muschelknautz E., Trefz M. : "Seceondary flow and short circuit flow at the dust discharge end of cyclone separators. Calculation and design of multicyclones", 1st European Symposium Separation of Particles from Gases, Nürnberg, 19.–21.4.1989, Preprints, pp. 345–362.

[32] Muschelknautz E., Trefz M. : "Design and Calculation of higher and highest loaded gas–cyclones", 2nd World Congress Particle Technology, Kyoto, Japan, 19.–22.9.1990, Preprints.

[33] Perić M. : "Ein zum Parallelrechnen geeignetes Finite–Volumen–Mehrgitterverfahren zur Berechnung komplexer Strömungen auf blockstrukturierten Gittern mit lokaler Verfeinerung", Abschlußbericht zum DFG–Vorhaben Pe 350/3–1 im DFG–Habilitandenstipendiumprogramm, Stanford University, USA, (1992).

[34] Schreck E., Perić M. : "Parallelization of implicit solution methods", ASME Fluids Engineering Conference, June 22–23, 1992, Los Angeles (CA), USA, (1992).

[35] Schneider J. : "Abscheideleistung eines symmetrischen Doppelzyklons", Research report of Luft– und Umwelt–Technik GmbH (LUT), Eckernförde, Germany, to be published in Chemie–Ingenieur–Technik, (1998).

[36] Sommerfeld M. : "Modelling of particle–wall collisions in confined gas–particle flows", Int. Journal of Multiphase Flows, Vol. 18, No. 6, pp. 905–926, (1992).

[37] Sommerfeld M. : "Modellierung und numerische Berechnung von partikelbeladenen turbulenten Strömungen mit Hilfe des Euler/Lagrange–Verfahrens", Berichte aus der Strömungstechnik, Shaker Verlag, Aachen, Germany, (1996).

[38] Stieß M. : "Mechanische Verfahrenstechnik", Bd. 1+2, Springer–Lehrbuch–Verlag, (1994).

[39] Seville J.P.K., Tüzün U., Clift R. : "Processing of Particulate Solids", Powder Technology Series, Blackie Academic & Professional, Chapman & Hall, London, (1997).

[40] Staudinger G., Obermaier St., Meisl Ch. : " Treffsicherheit und Zuverlässigkeit der heutigen Zyklonberechnung", VDI–Berichte 1511, VDI–Verlag, Düsseldorf, pp. 1–23, (1999).

[41] Ter Linden A. J. : "Investigations into Cyclone Dust Collectors", Proc. Inst. Mech. Eng., pp. 160–233, (1949).

[42] Trefz M. : "Die verschiedenen Abscheidevorgänge im höher und hoch beladenen Gaszyklon unter besonderer Berücksichtigung der Sekundärströmung", VDI–Fortschritts–Berichte, Reihe 3 : Verfahrenstechnik, Nr. 295, VDI–Verlag Düsseldorf, (1992).

[43] Tsuji Y., Oshima T., Morikawa Y. : "Numerical simulation of pneumatic conveying in a horizontal pipe", KONA – Powder Science and Technology in Japan, No. 3, pp. 38–51, (1985).

[44] Tsuji Y., Shen N.Y., Morikawa Y. : "Lagrangian Simulation of Dilute Gas–Solid Flows in a Horizontal Pipe", Advanced Powder Technology, Vol. 2, No. 1, pp. 63–81, (1991).

[45] VDI–Wärmeatlas, "Zyklone zur Abscheidung von Feststoffen aus Gasen", VDI–Gesellschaft Verfahrenstchnik und Chemieingenieurwesen (GVC), 8. Auflage, Springer-Verlag, pp. Lja1–Lja11, (1997).

[46] VDI–Richtlinie "VDI 3676 — Massenkraftabscheider", VDI–Handbuch Reinhaltung der Luft, Band 6, Register-Nr. 10, pp. 1–16, (Mai 1980).

[47] VDI–Gesellschaft Energietechnik : Zyklonabscheider in der Energie– und Verfahrenstechnik, Tagung Essen, 29.–30. Oktober 1996, VDI–Berichte 1290, VDI–Verlag, Düsseldorf, (1996).

[48] VDI–Gesellschaft Energietechnik : Zyklonabscheider in der Energie– und Verfahrenstechnik, Tagung Leverkusen, 27.–28. Oktober 1999, VDI–Berichte 1511, VDI–Verlag, Düsseldorf, (1999).

[49] Web site of the Research Group on Multiphase Flow, University of Technology, Chemnitz, Germany.
http://www.tu-chemnitz.de/mbv/FAK/TechnThDyn/mpf/e/index.html – Index.
http://www.tu-chemnitz.de/mbv/FAK/TechnThDyn/mpf/mpf_lit.html – List of Publications.

[50] Wieck T., Hofeditz U. : "Konstruktion und Fertigung unterschiedlicher Varianten von Zyklonabscheidern — Experimenteller Vergleich der Abscheideleistung", Diploma thesis, Flensburg University of Applied Sciences, (1997).

Figure 1: Diagram of the standard cylinder-on-cone design of cyclone separators.

a) b) c)

Figure 2: Ter Linden's [41] measurements of gas velocity field in a standard reverse flow cyclone with tangential inlet : a) tangential, b) radial and c) axial velocity components.

a)

b) c)

Figure 3: Different cyclone designs for industrial applications. a) Fixed impeller through–flow (Strauss, 1975); b) axial entry reverse flow (Strauss, 1975); c) tangential entry reverse flow (Inst. of Chem. Engineers, 1985).

a) b)

c)

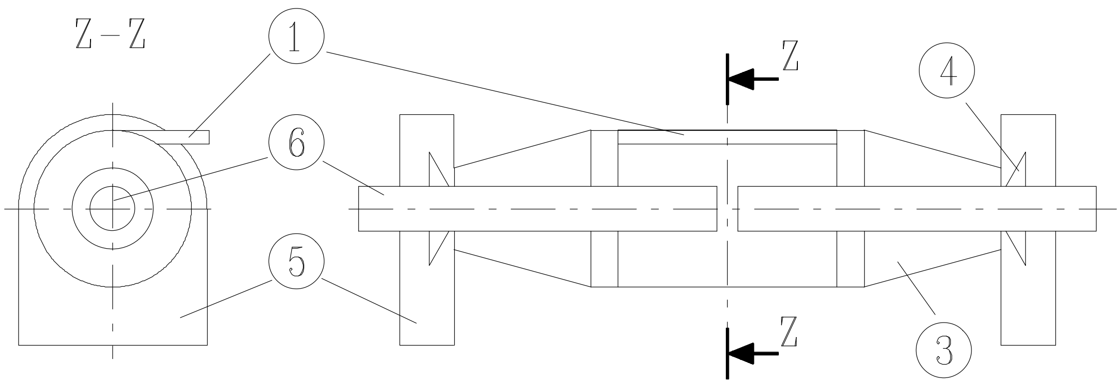


Figure 4: Examples of cyclone designs. a) axial multi-cyclone; b) swirling flow particle separator; c) symmetrical double cyclone (LUT GmbH, 1998).

Figure 5: Gas flow and particle separation in a standard cyclone with tangential inflow.

Figure 6: Typical example of a fractional or grade efficiency curve for a standard cyclone; curve a) for tangential inflow standard cyclone; curve b) for axial inflow cyclone.

Figure 7: Schematic view of the geometry of a standard cyclone with tangential inflow.

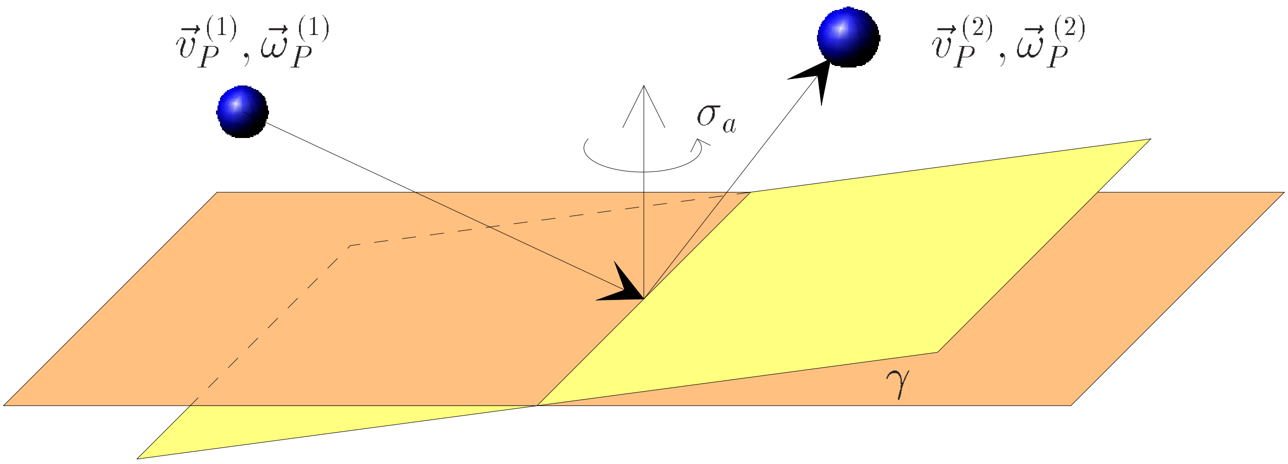


Figure 8: Particle–wall collision of a spherical particle with an inclined "virtual" wall.

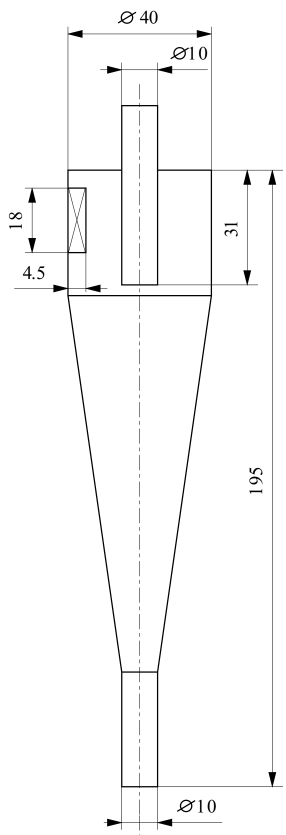


Figure 9: Schematic view of the Z10 standard cyclone of König [19].

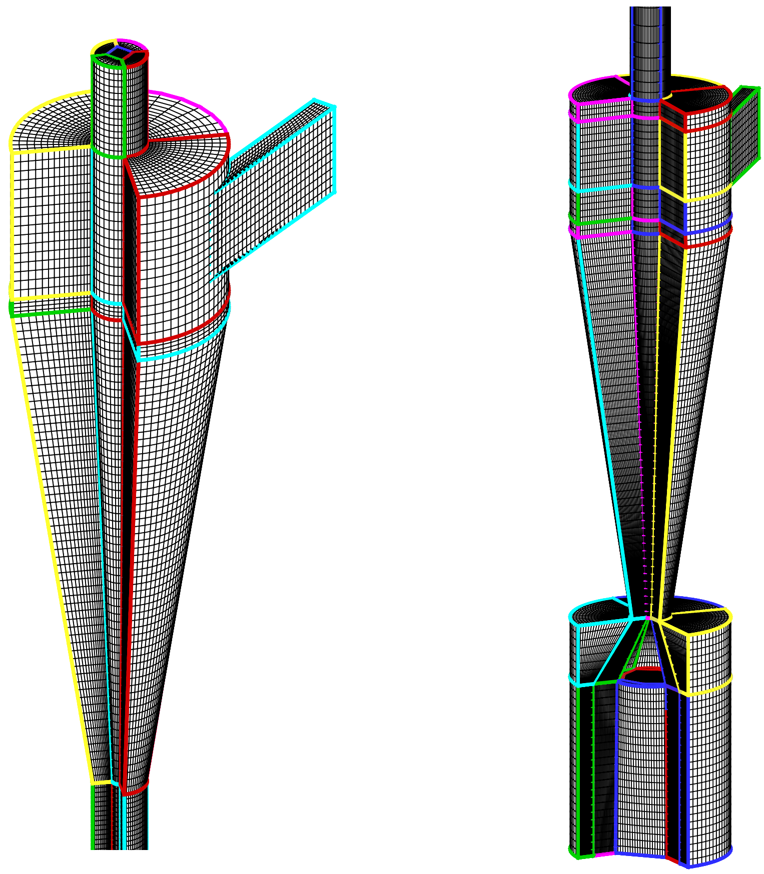

Figure 10: Numerical meshes for the Z10 standard cyclone.

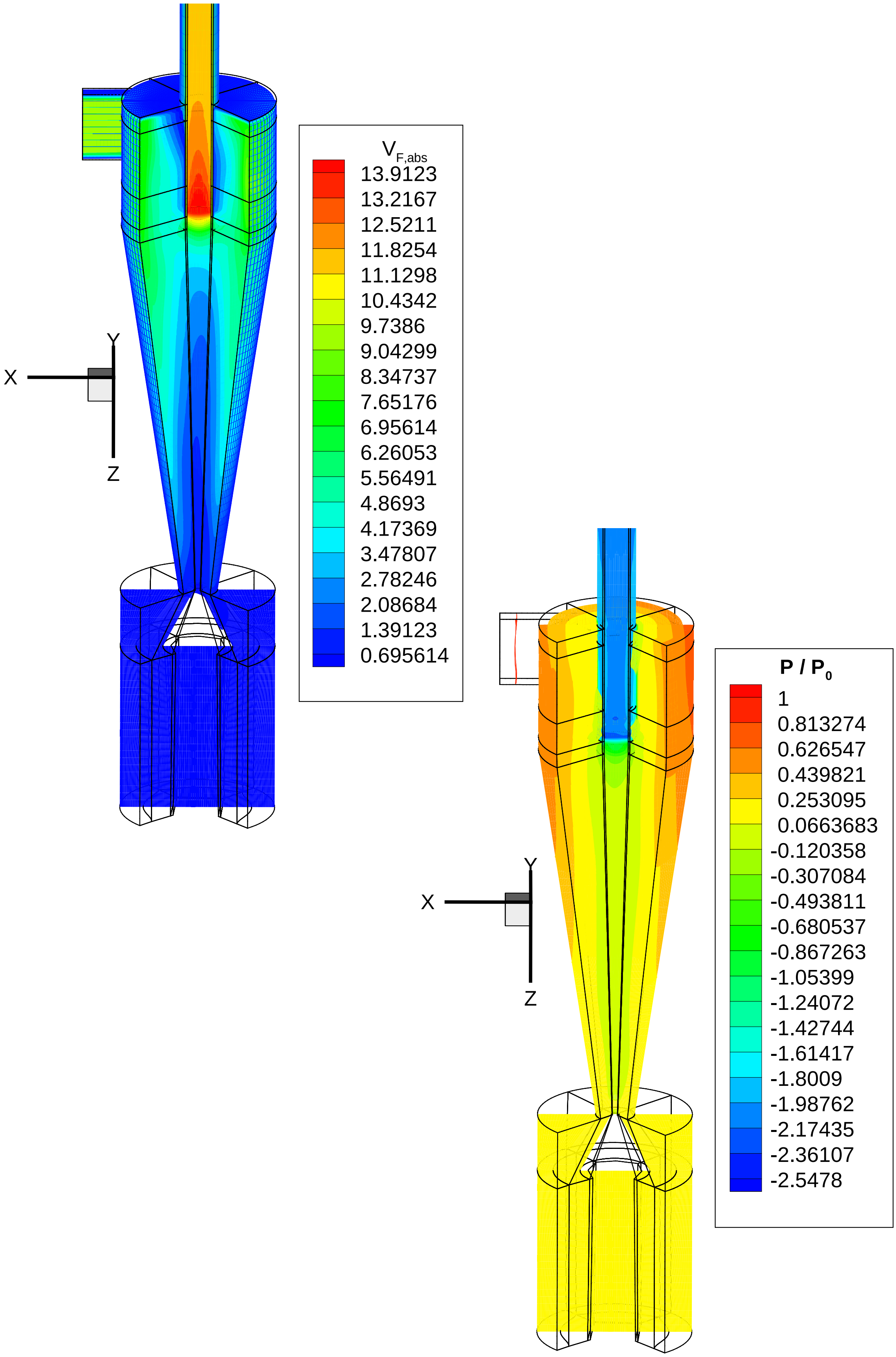


Figure 11: Distribution of the absolute gas velocity and pressure in the Z10 cyclone for $u_{F,in} = 10\ m/s$.

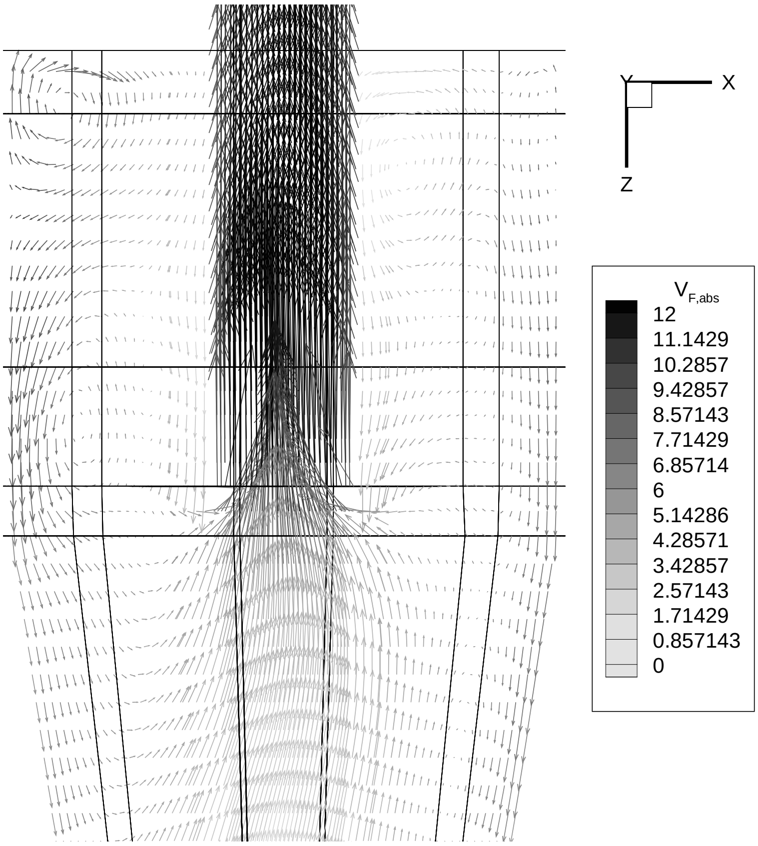


Figure 12: Gas velocity distribution in the upper part of the Z10 cyclone for $u_{F,in}$ = $10\ m/s$ (x–z–plane).

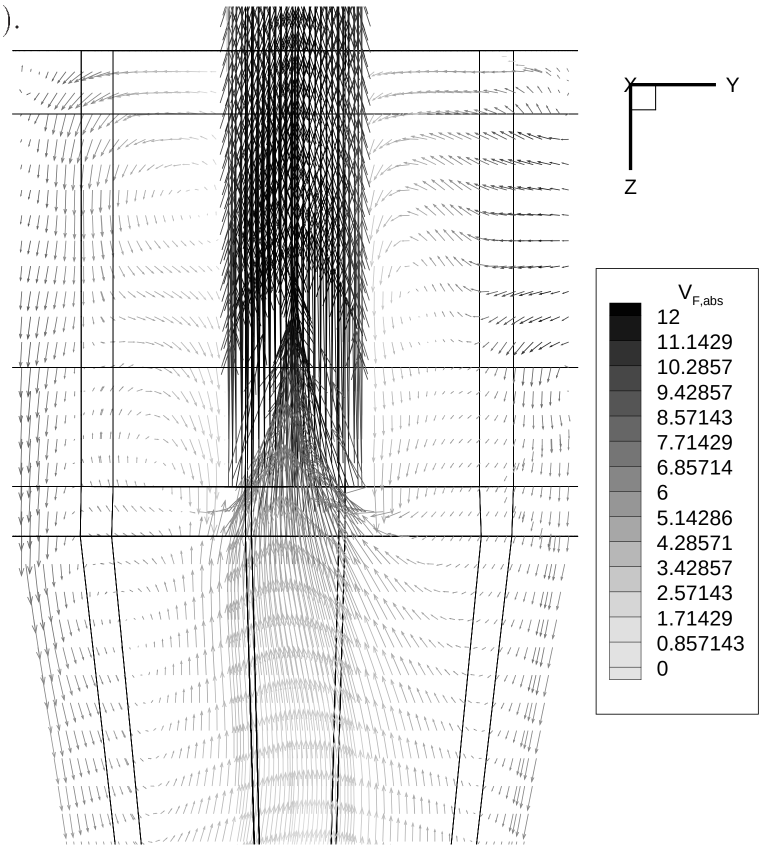


Figure 13: Gas velocity distribution in the upper part of the Z10 cyclone for $u_{F,in}$ = $10\ m/s$ (y–z–plane).

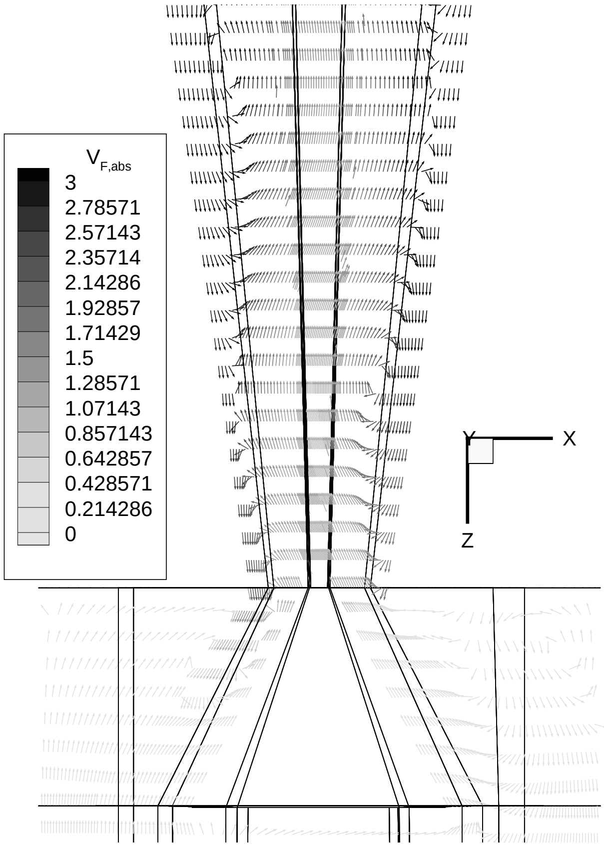


Figure 14: Gas velocity distribution in the vicinity of the apex cone in Z10 cyclone for $u_{F,in} = 10\ m/s$ (x–z–plane).

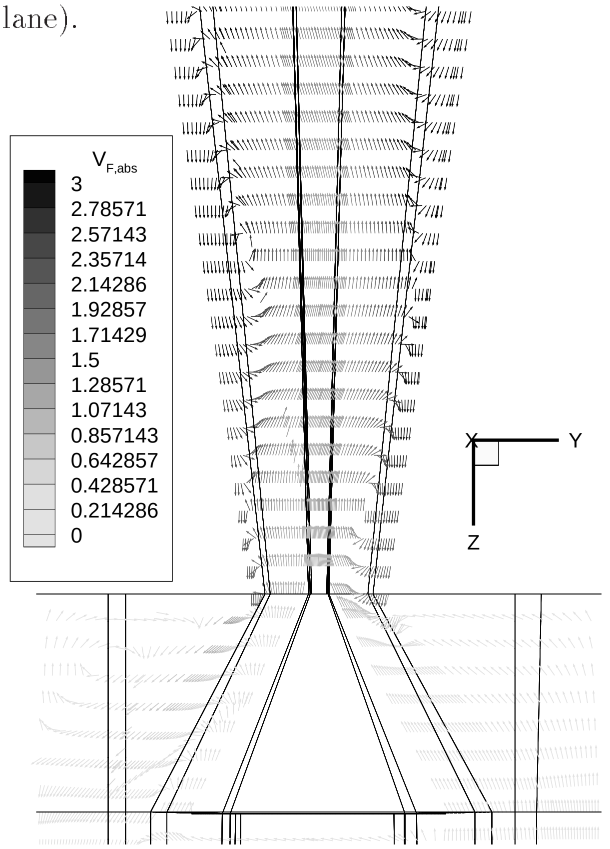


Figure 15: Gas velocity distribution in the vicinity of the apex cone in Z10 cyclone for $u_{F,in} = 10\ m/s$ (y–z–plane).

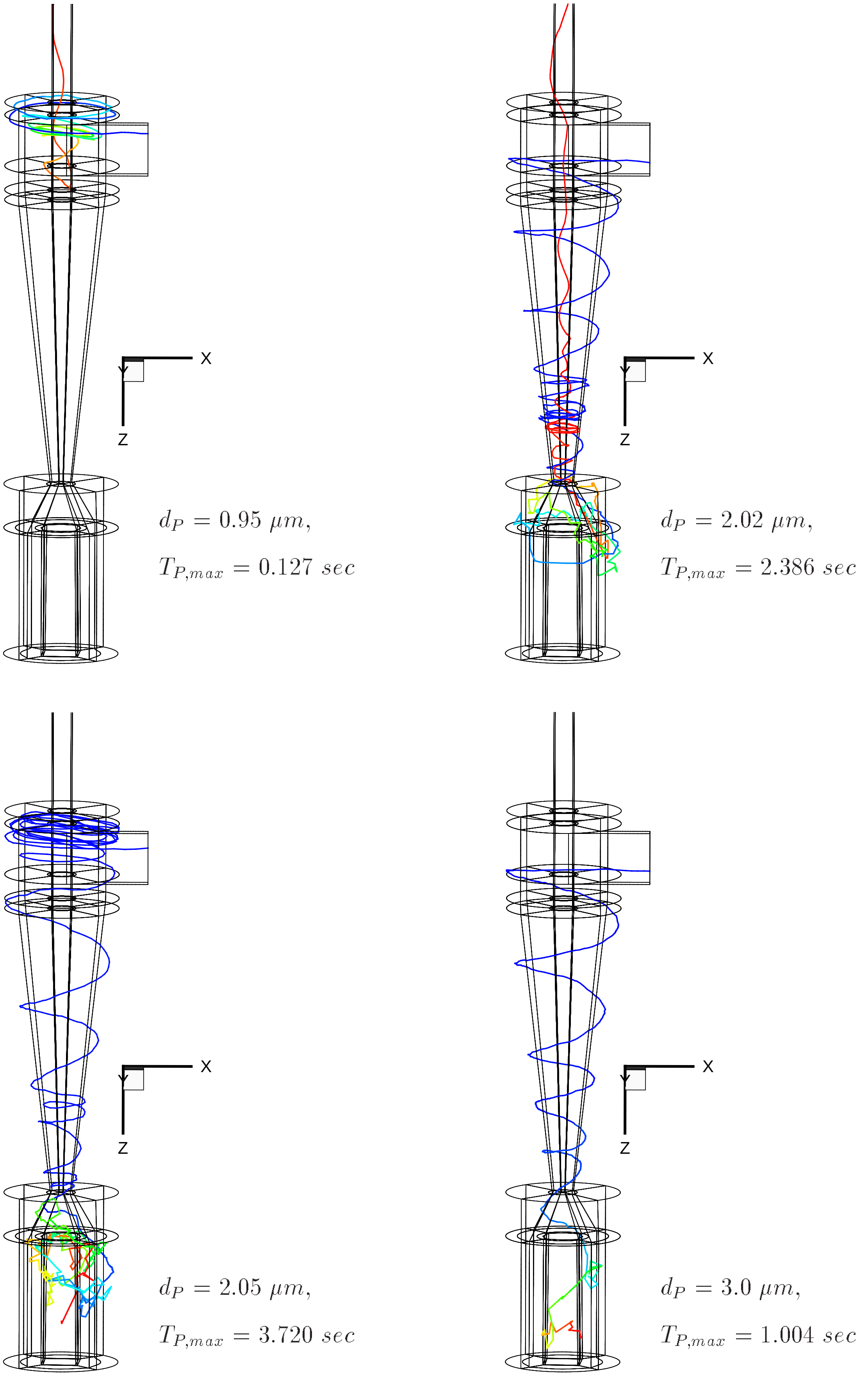


Figure 16: Particle trajectories of different particle diameter in the Z10 cyclone (color represents the particle residence time; $\rho_P = 2500\ kg/m^3$).

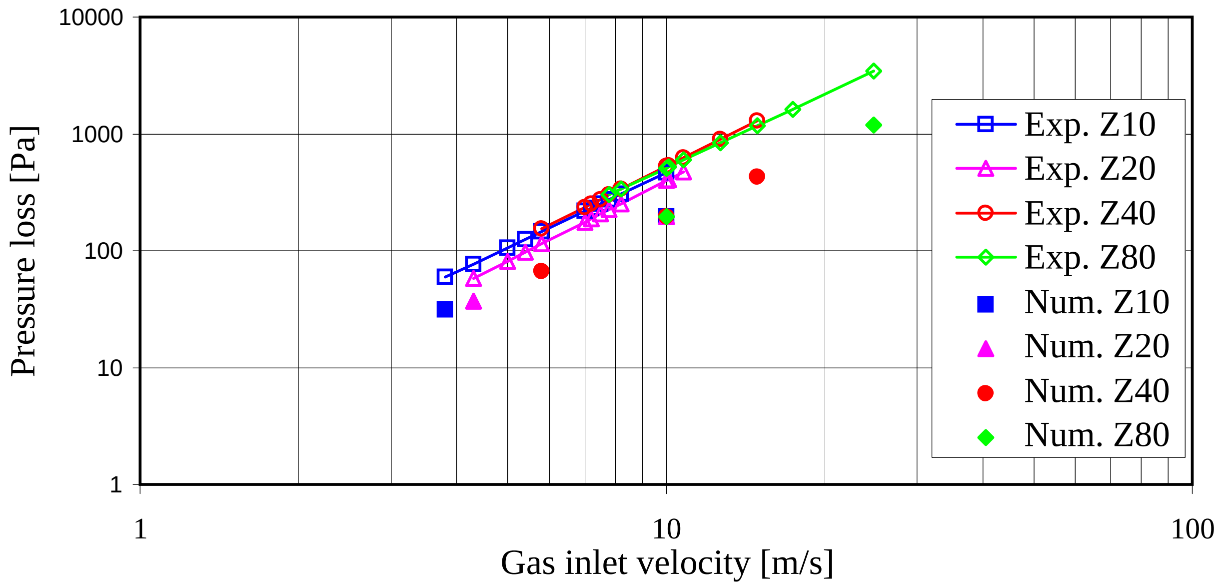


Figure 17: Comparison of predicted pressure loss over the Z10,...,Z80 cyclone for various gas inlet velocities with experimental data of König [19].

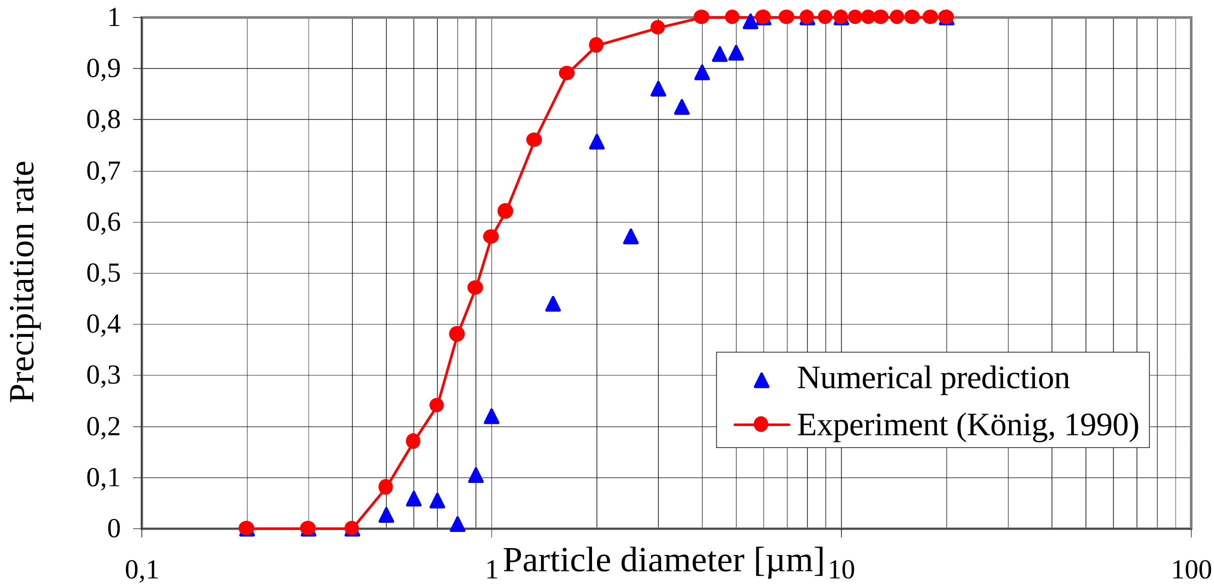


Figure 18: Comparison of the separation rate for the Z10 cyclone, $u_F = 10\ m/s$.

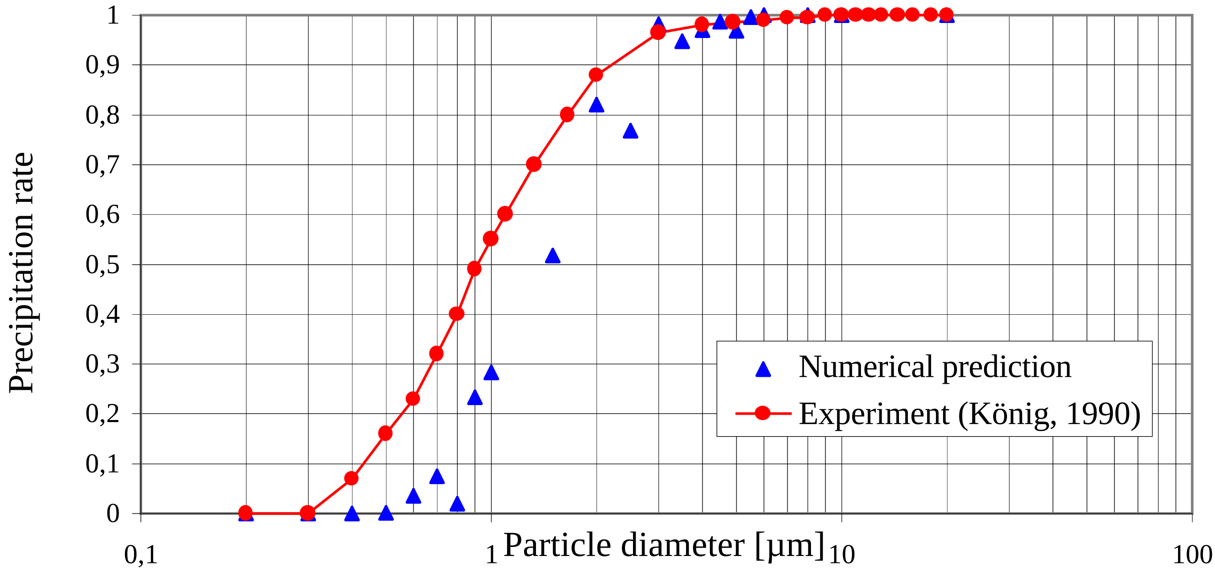


Figure 19: Comparison of the separation rate for the Z20 cyclone, $u_F = 10\ m/s$.

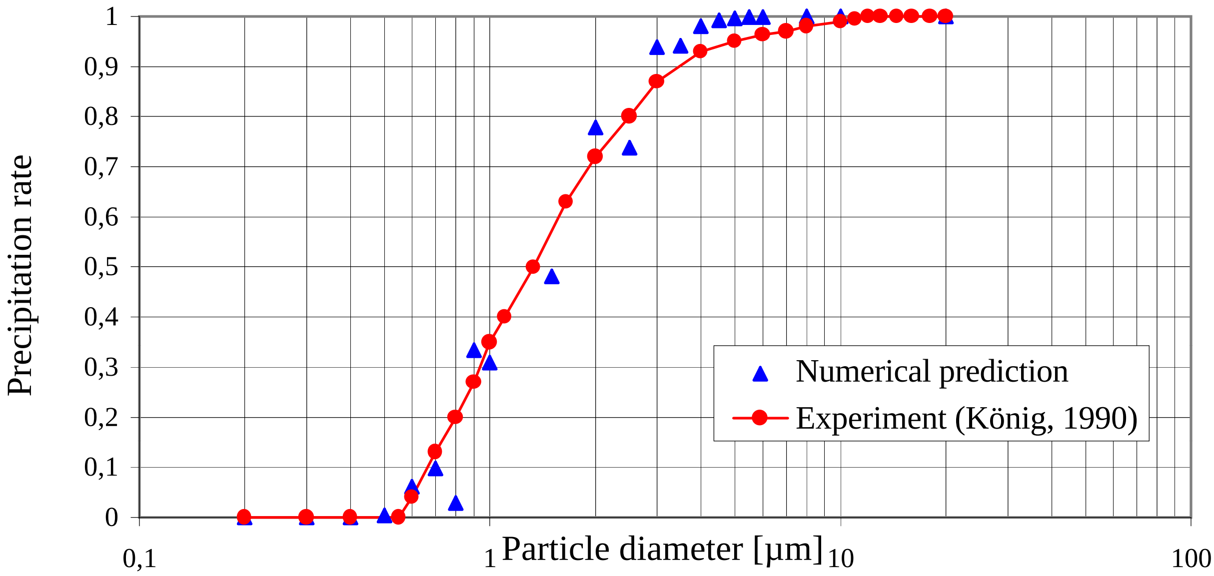


Figure 20: Comparison of the separation rate for the Z40 cyclone, $u_F = 10\ m/s$.

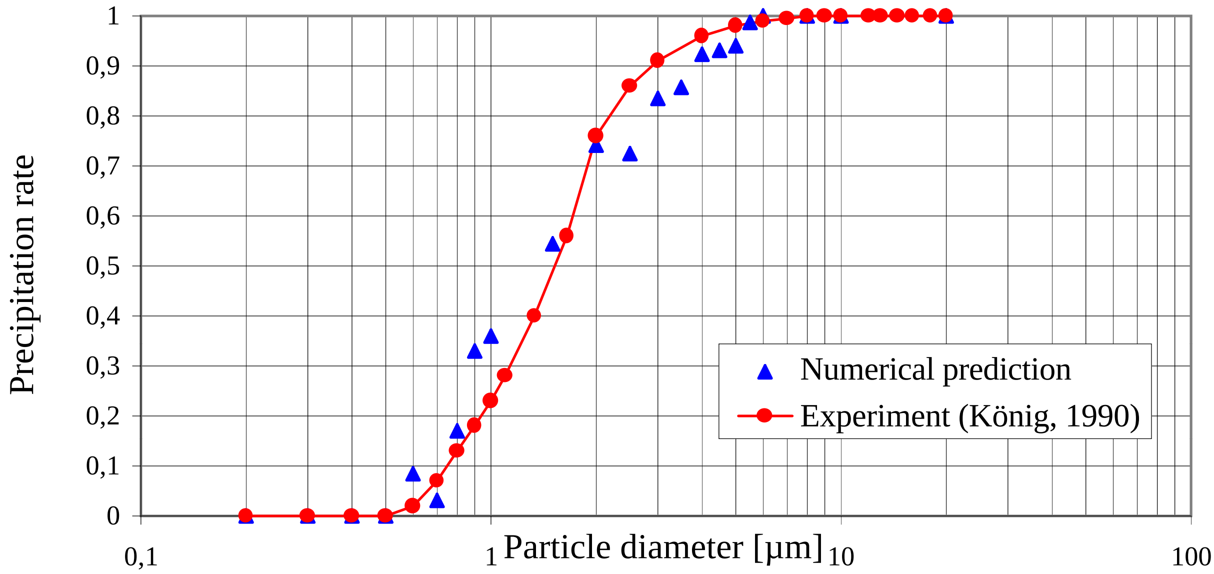


Figure 21: Comparison of the separation rate for the Z80 cyclone, $u_F = 10\ m/s$.

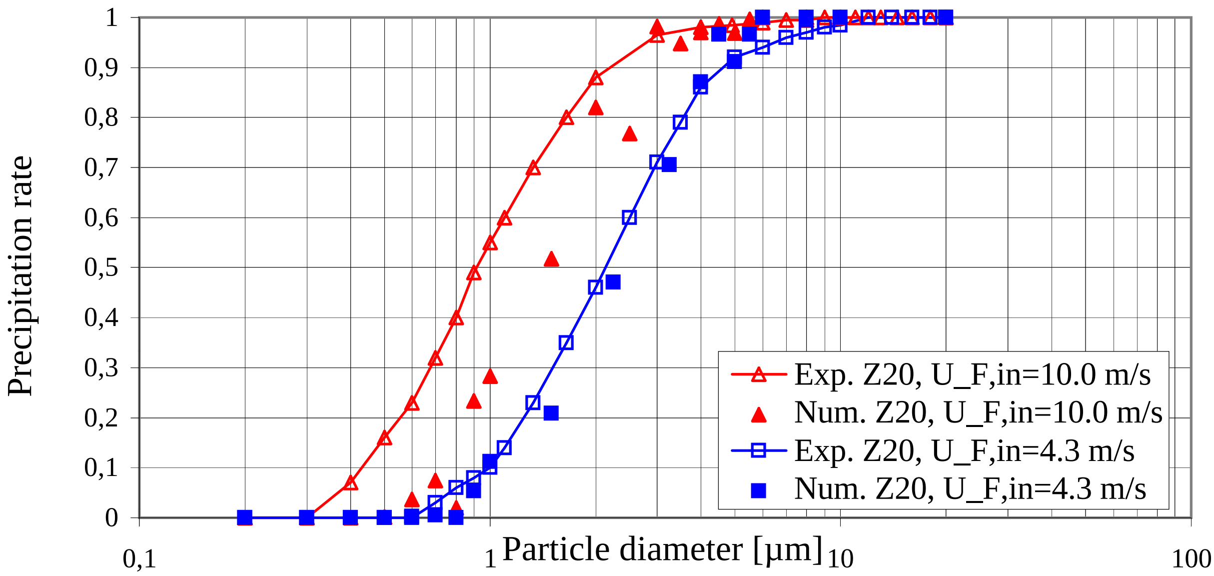


Figure 22: Comparison of separation rates for Z20 and gas inlet velocities $u_F = 4.3\ m/s$ and $10\ m/s$.

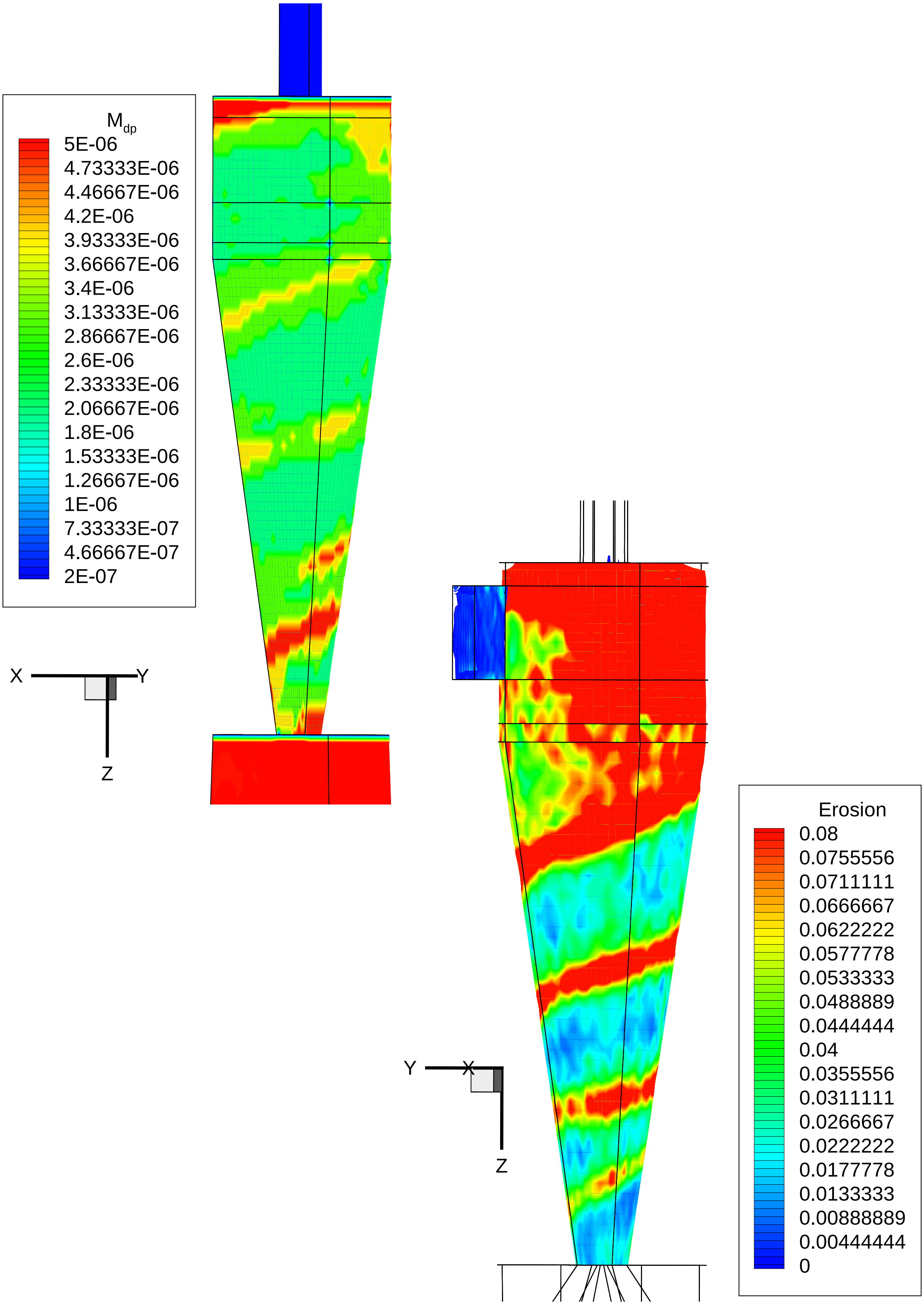


Figure 23: Distribution of the mean particle diameter and the predicted particle erosion intensity for the Z10 cyclone ($u_{F,in} = 10\ m/s$).

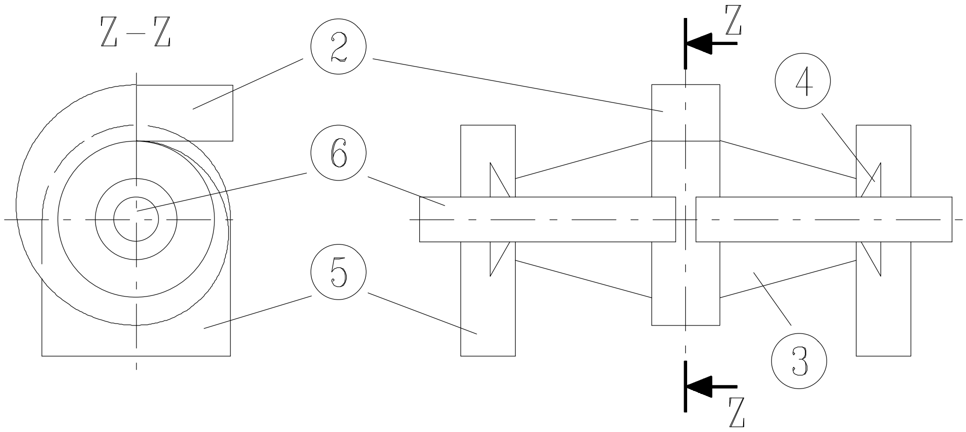


Figure 24: Symmetrical double cyclone with spiral inlet (ZS).

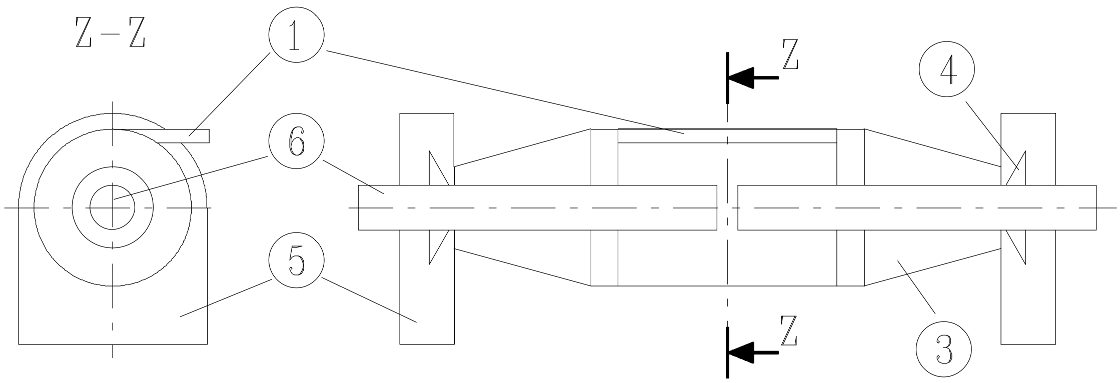


Figure 25: Symmetrical double cyclone with tangential inlet (ZT).

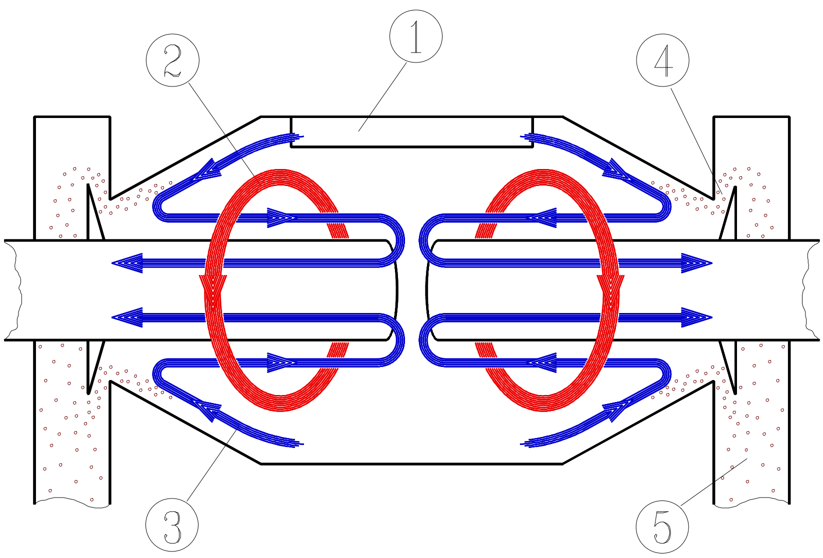


Figure 26: Functional diagram of the symmetrical double cyclone separator.

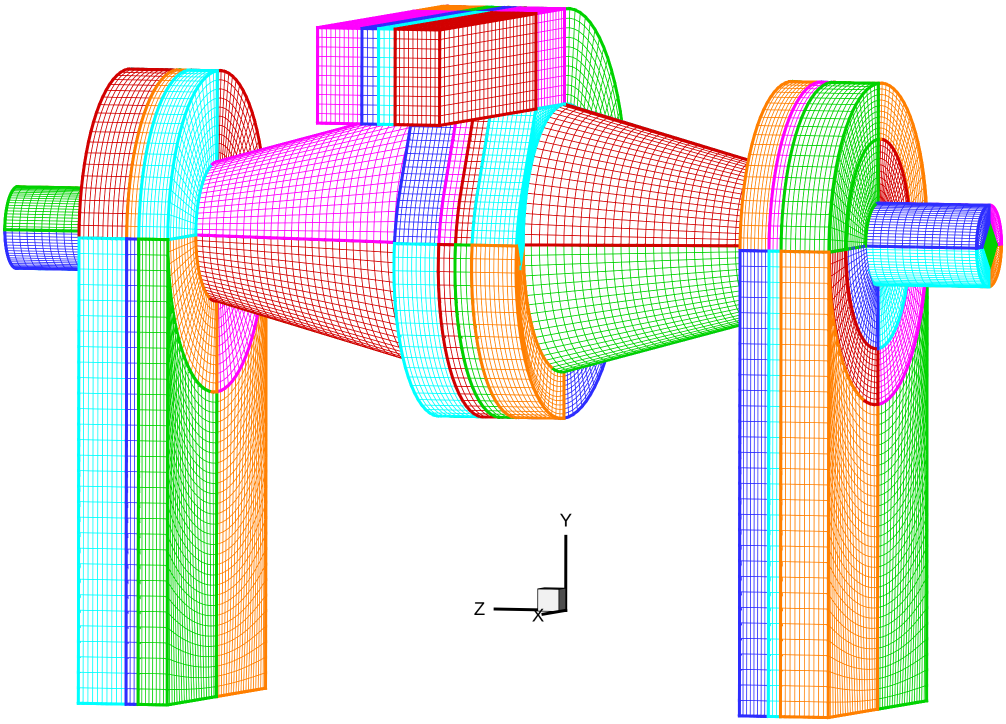


Figure 27: Structure of the numerical mesh for the symmetrical double cyclone ZS30 with spiral inflow and a gap width at the apex cone of $h_{ac} = 30\ mm$.

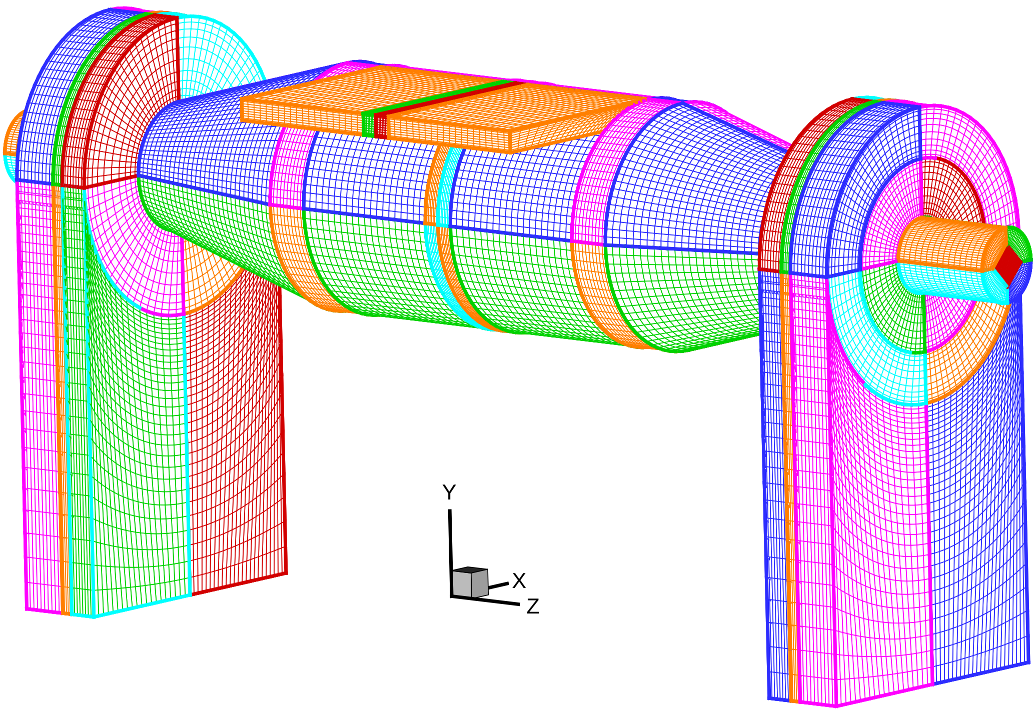


Figure 28: Structure of the numerical mesh for the symmetrical double cyclone ZT30 with tangential inflow and a gap width at the apex cone of $h_{ac} = 30\ mm$.

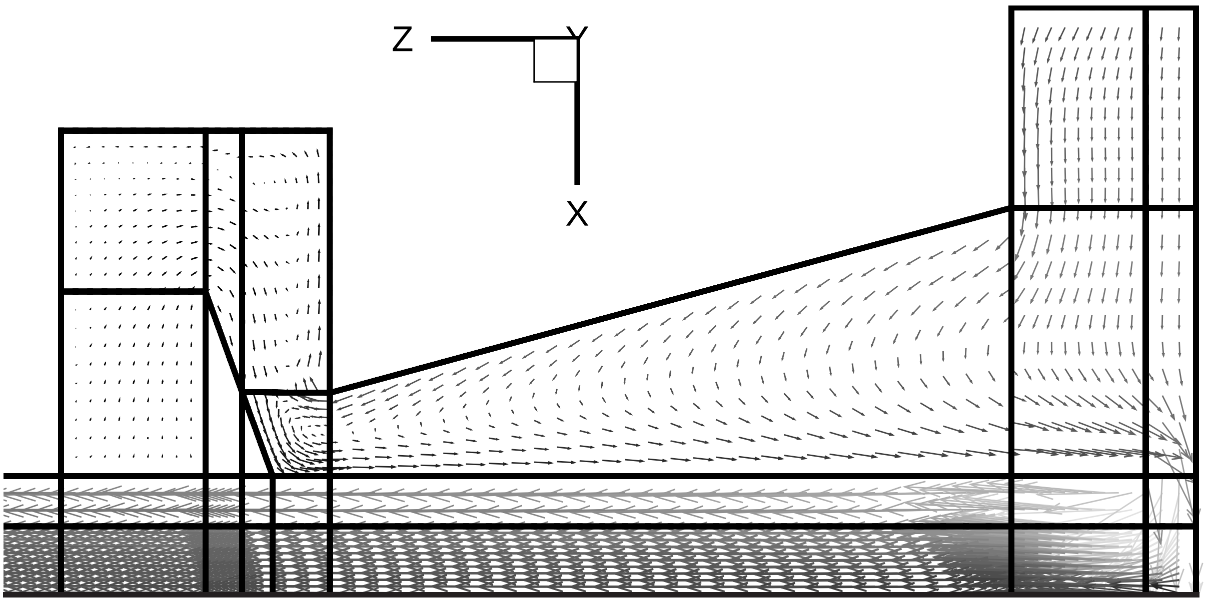


Figure 29: Distribution of gas velocity for ZS30 in the x–z–plane.

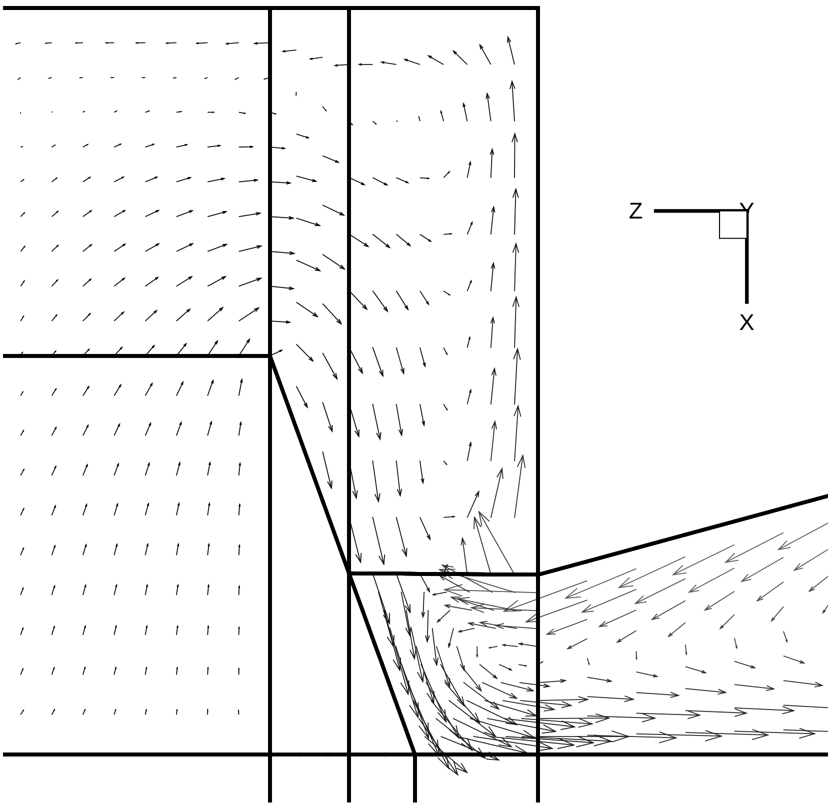


Figure 30: Detail of gas velocity distribution in ZS30 in the vicinity of the apex cone (x–z–plane).

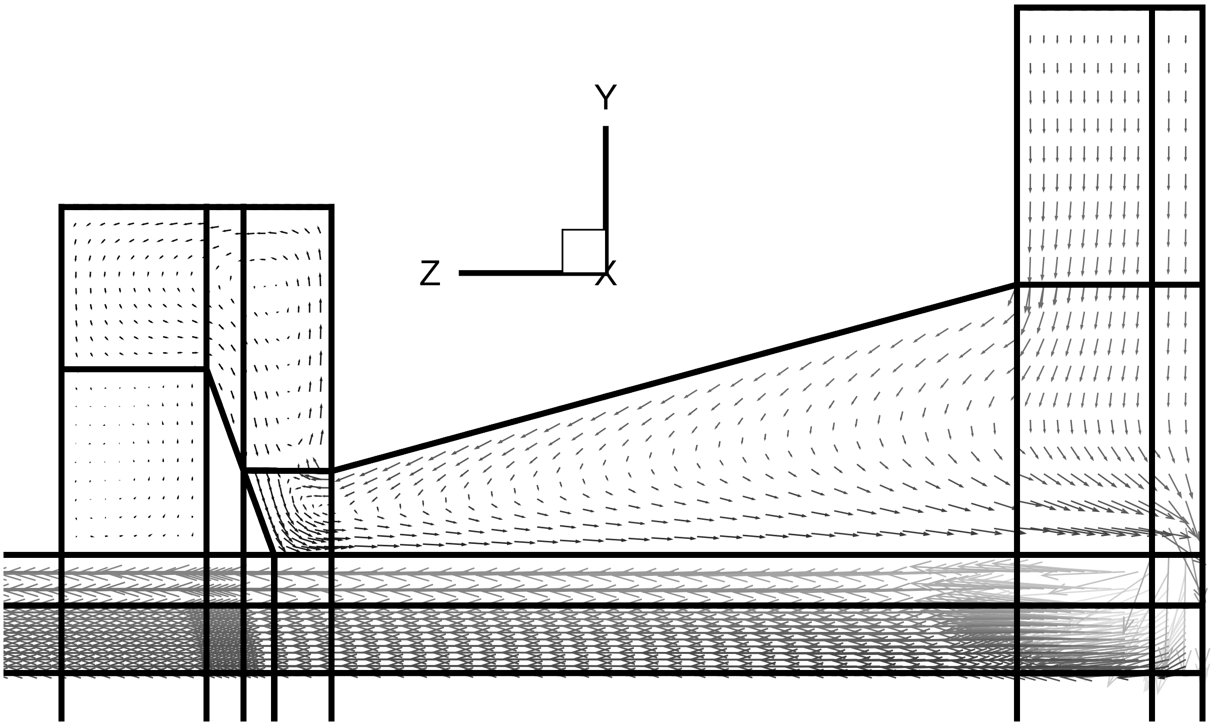


Figure 31: Distribution of gas velocity for ZS30 in the y–z–plane.

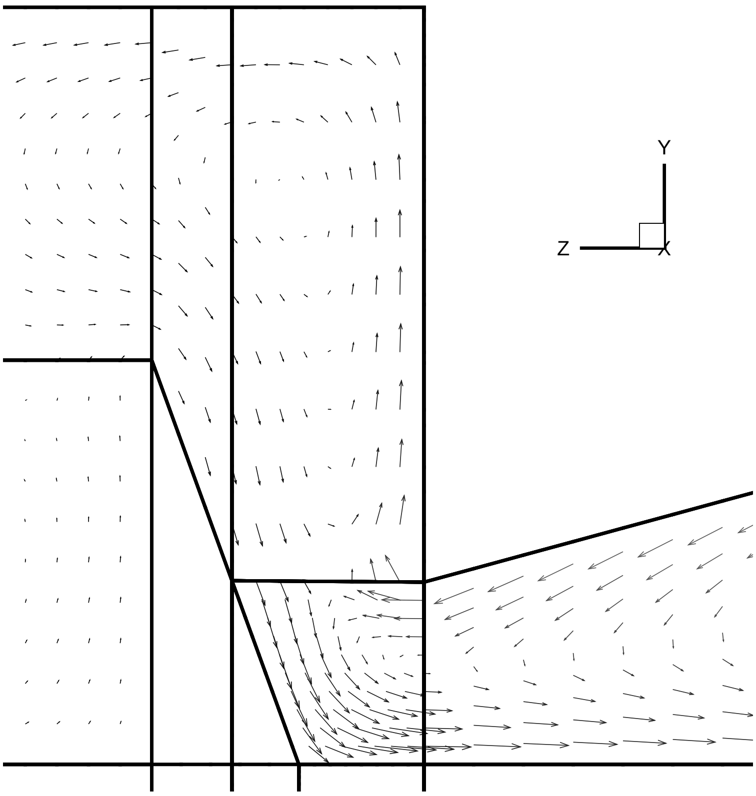


Figure 32: Detail of gas velocity distribution in ZS30 in the vicinity of the apex cone (y–z–plane).

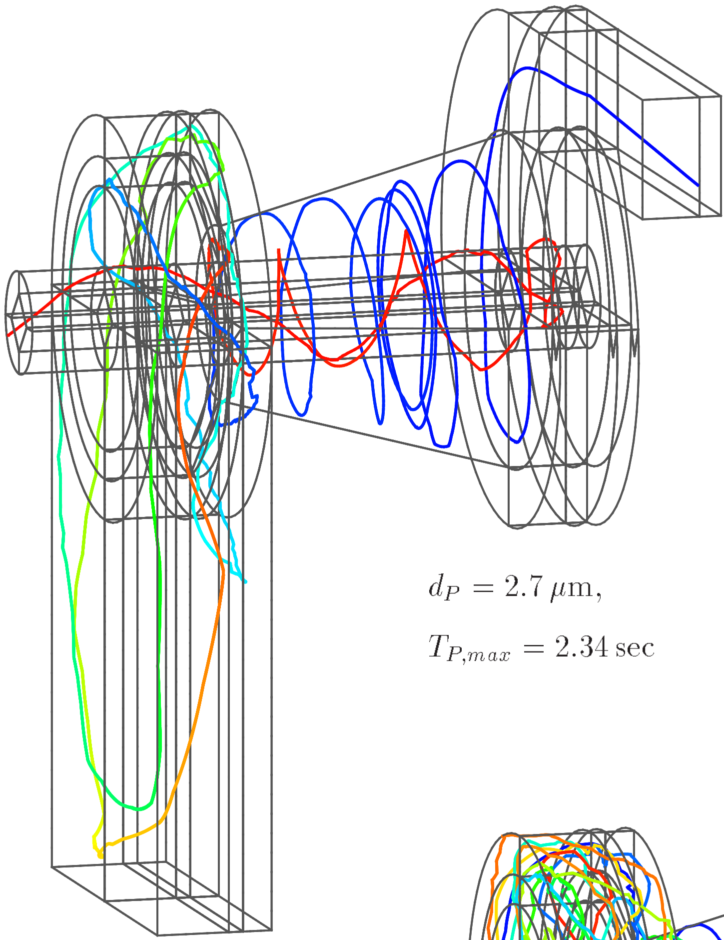

$d_P = 2.7\,\mu\text{m}$,

$T_{P,max} = 2.34\,\text{sec}$

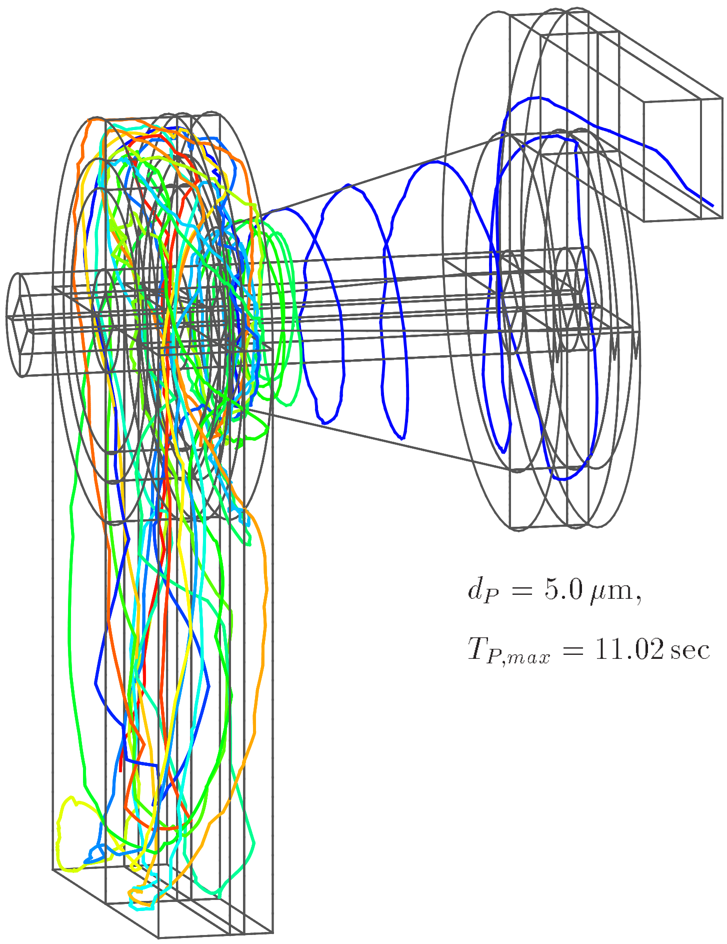

$d_P = 5.0\,\mu\text{m}$,

$T_{P,max} = 11.02\,\text{sec}$

Figure 33: Particle trajectories in the symmetrical double cyclon ZS18 with a gap width at the apex cone of $h_{ac} = 18\ mm$ (color of particle track corresponds to the particle residence time in the cyclone).

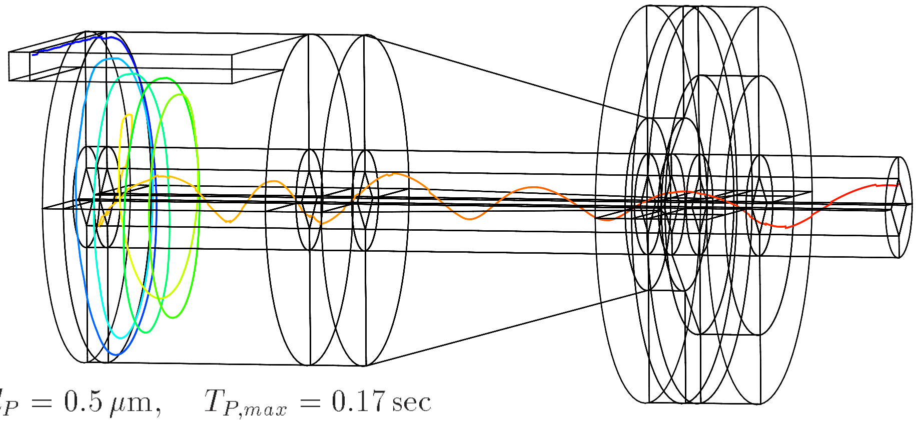

$d_P = 0.5\,\mu\text{m}, \quad T_{P,max} = 0.17\,\text{sec}$

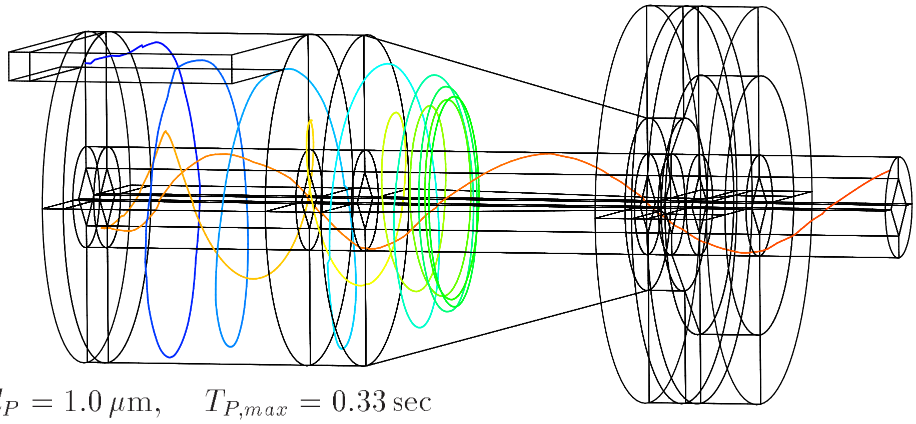

$d_P = 1.0\,\mu\text{m}, \quad T_{P,max} = 0.33\,\text{sec}$

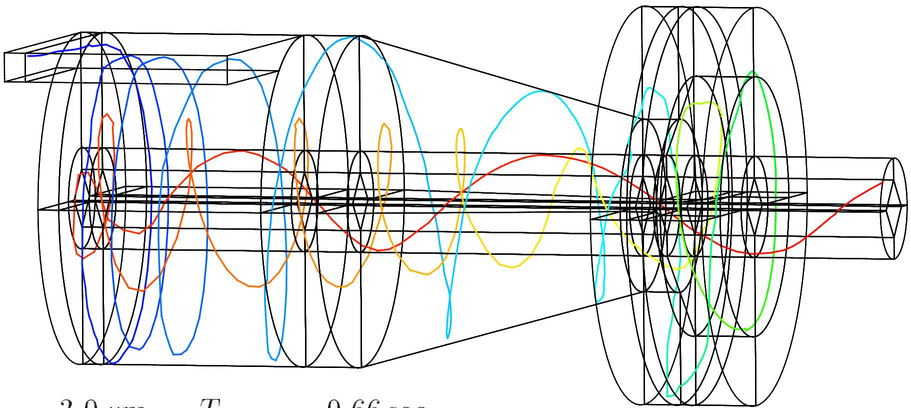

$d_P = 3.0\,\mu\text{m}, \quad T_{P,max} = 0.66\,\text{sec}$

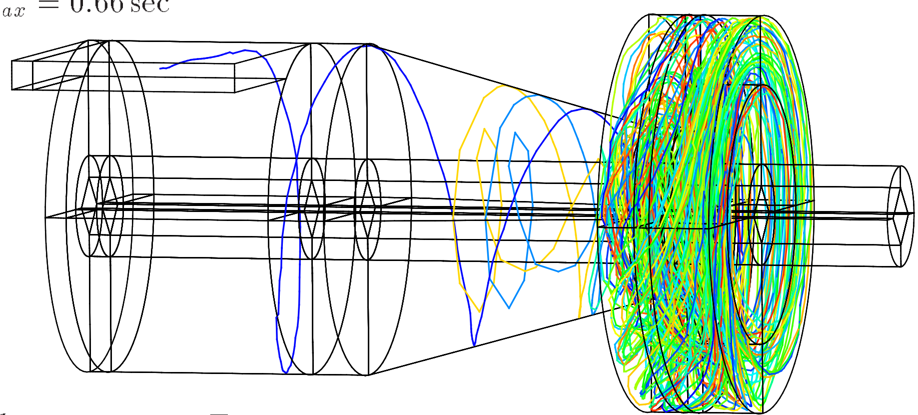

$d_P = 6.0\,\mu\text{m}, \quad T_{P,max} = 19.85\,\text{sec}$

Figure 34: Particle trajectories in the symmetrical double cyclon ZT30.

(a) 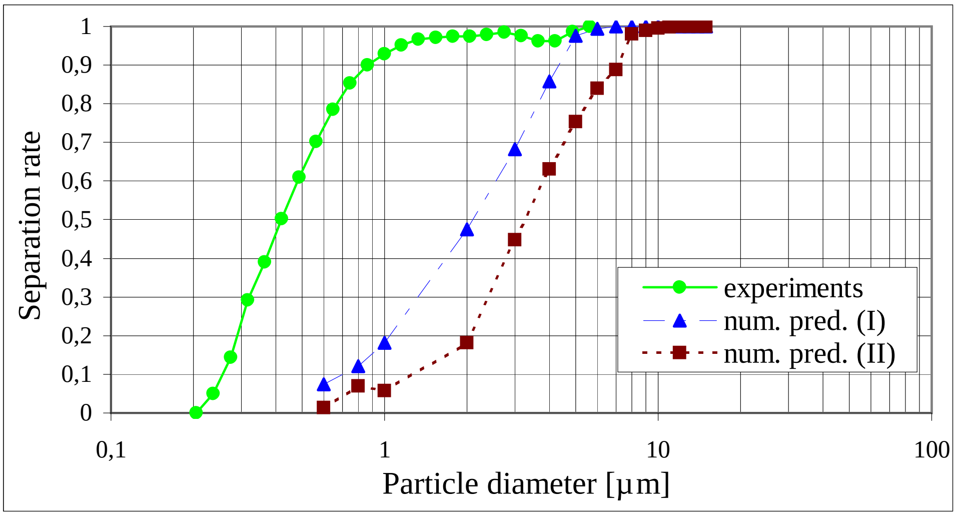


(b) 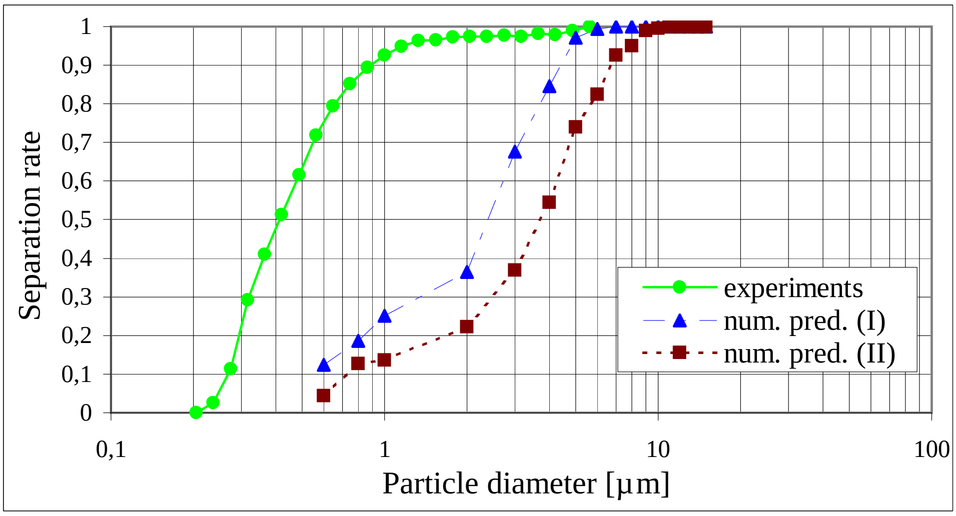


(c) 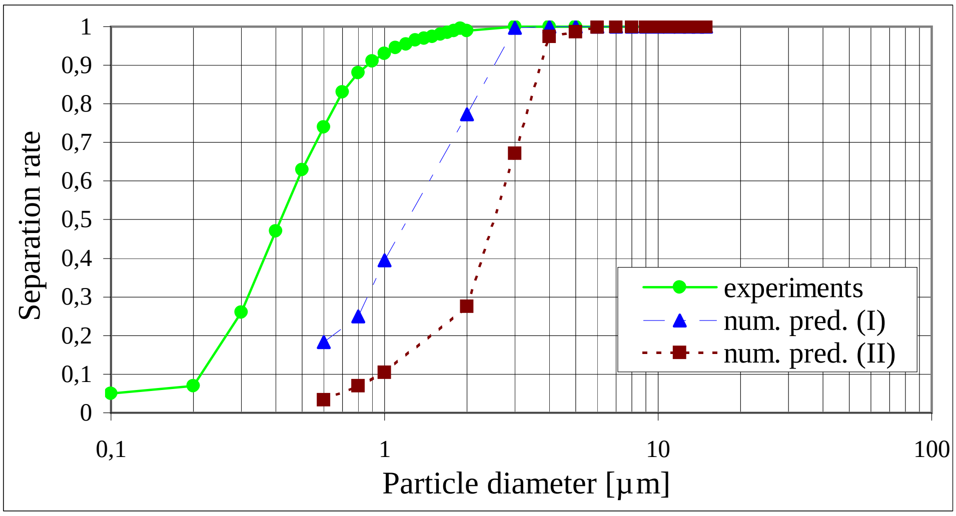


Figure 35: Comparison of numerical predicted particle separation efficiency with experimental data for

(a) ZS18 with $h_{ac} = 18.7\,\mathrm{mm}$ and $u_{F,in} = 25.0\,\mathrm{m/s}$
(b) ZS30 with $h_{ac} = 30.0\,\mathrm{mm}$ and $u_{F,in} = 25.0\,\mathrm{m/s}$
(c) ZT30 with $h_{ac} = 30.0\,\mathrm{mm}$ and $u_{F,in} = 25.0\,\mathrm{m/s}$

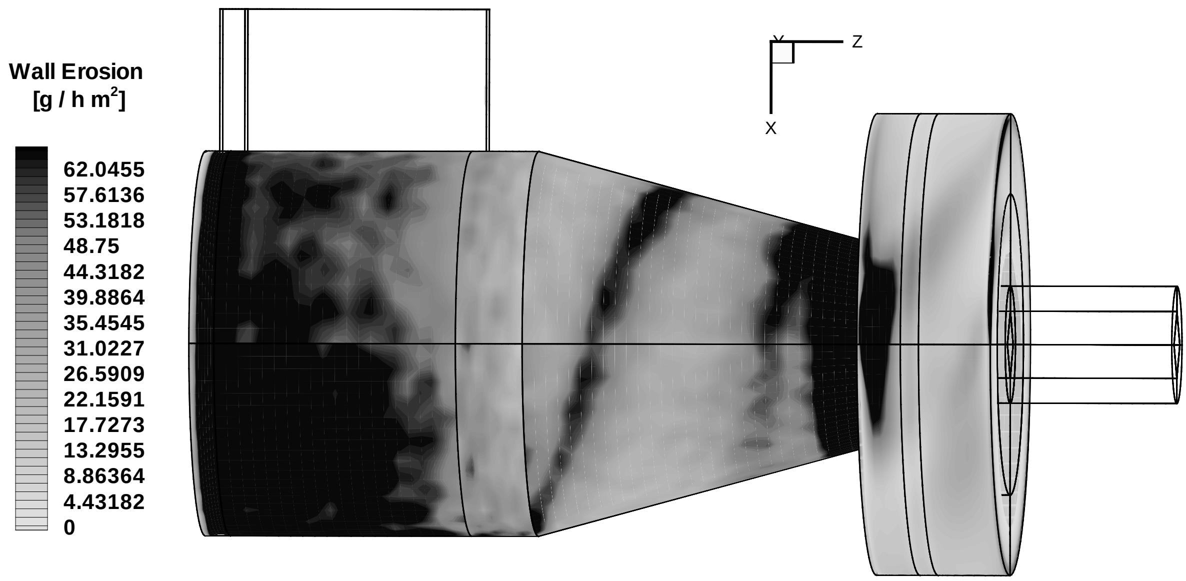


Figure 36: Visualization of spiral particle rope separating from the edge of the tangential inflow in the erosion pattern on the conical cyclon walls.

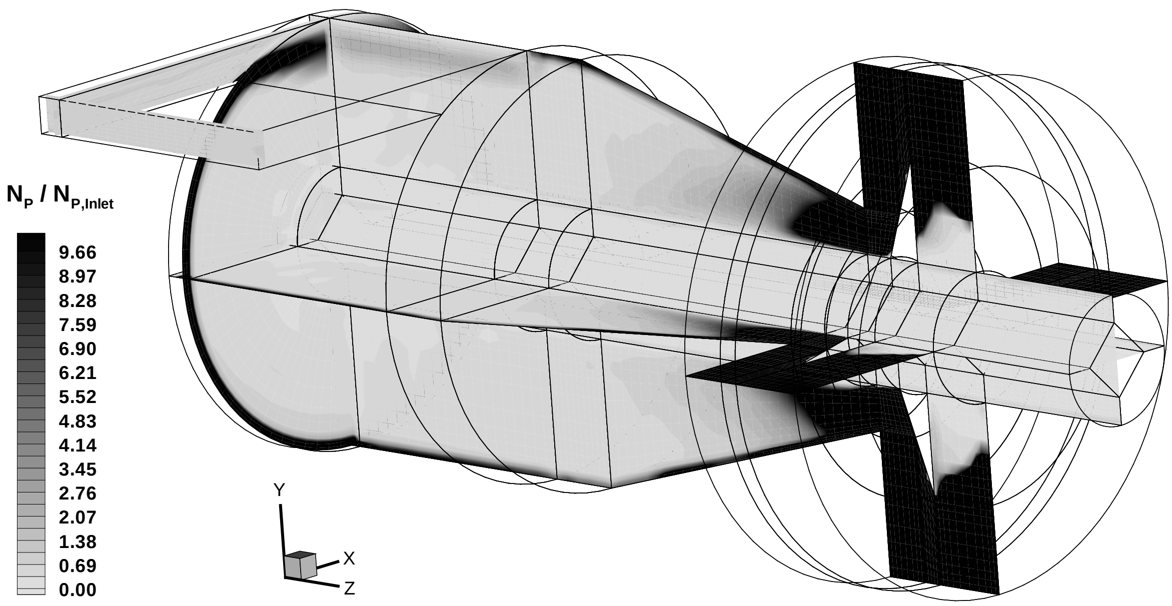


Figure 37: Distribution of relative particle number density in symmetrical double cyclon ZT30.